

Universitat Politècnica de Catalunya

## Treball Final de Grau en Enginyeria Física

# Turbulence transition in pulsatile pipe flow: shear-thinning effects



CENTER OF  
APPLIED SPACE TECHNOLOGY  
AND MICROGRAVITY



ZARM - University of Bremen

June 2021

**Author:** Laura Dot Casadevall

**Director:** Prof. Dr. Marc Ávila

**Codirector:** Dr. Álvaro Meseguer

**Supervisor:** Daniel Morón

## Acknowledgements

I would like to express my gratefulness to Prof. Dr. Marc Ávila for allowing me to join the Center of Applied Space Technology and Microgravity (ZARM) at University of Bremen and encouraged me to keep researching on pipe flow and turbulence transition topic. Moreover, I would really like to thank Daniel Morón, who has always helped me with everything I needed, no matter what and when, and he has supervised my work better than ever.

I would like to extend my gratefulness to the other research group members for sharing their points of view and different questions about this work topic, as this has uncovered other perspectives to address the problem.

Finally, I also want to thank my co-director Dr. Álvaro Meseguer from Universitat Politècnica de Catalunya (UPC), given that his lessons on Numerical and Computational Methods, plus Physics of Fluids inspired me to choose this bachelor's thesis topic and he helped me to contact Prof. Dr. Marc Ávila.

## Notation dictionary

$t$	time
$\mathbf{u}=(u,v,w)$	velocity field
$\rho$	density
$p$	pressure
$\tau$	shear stress tensor
$\nu$	kinematic viscosity
$\mu$	viscosity
$\hat{\mu}_{\infty}$	infinite shear-rate viscosity
$\hat{\mu}_0$	zero shear-rate viscosity
$\hat{\lambda}$	fluid's time constant
$n_c$	shear-thinning index
$a$	shift term
$Re$	Reynolds number
$Wo$	Womersley number
$w$	pulsation angular frequency
$A$	pulsation amplitude
$R$	pipe radius
$D$	pipe diameter
$N$	number of radial nodes
$\alpha$	axial wavenumber
$\beta$	azimuthal wavenumber
$G$	energy gain

# Contents

<b>Abstract</b>	<b>6</b>
<b>1 Introduction</b>	<b>7</b>
1.1 Motivation and state of the art . . . . .	7
1.2 Objectives . . . . .	7
<b>2 Description of the problem</b>	<b>8</b>
2.1 Non-Newtonian Fluids . . . . .	8
2.1.1 Carreau-Yasuda model . . . . .	9
2.2 Governing equations . . . . .	10
<b>3 Base Flow</b>	<b>12</b>
3.1 Steady Base Flow . . . . .	12
3.1.1 Chebyshev discretization . . . . .	13
3.1.2 Iterative Newton's method . . . . .	14
3.2 Unsteady Base Flow . . . . .	15
<b>4 Transient Growth Analysis (TGA)</b>	<b>17</b>
4.1 Disturbance and linearized Navier-Stokes equations . . . . .	17
4.2 Theoretical fundamentals . . . . .	19
4.2.1 Linear stability . . . . .	19
4.2.2 Transient Growth assessment . . . . .	19
4.3 Improved Projection Scheme (IPS) . . . . .	20
4.3.1 IPS for Newtonian fluids . . . . .	20
4.3.2 IPS for non-Newtonian fluids . . . . .	22
<b>5 Convergence Analysis</b>	<b>23</b>
<b>6 Results and discussion</b>	<b>27</b>
6.1 Base flow analysis . . . . .	27
6.2 TGA results . . . . .	32
<b>7 Conclusions</b>	<b>37</b>
<b>References</b>	<b>38</b>

## List of Figures

1	Fluid behaviour according to (a) shear stress, (b) viscosity vs shear rate relation . . . . .	8
2	Carreau viscosity profile . . . . .	10
3	Steady base flow validation . . . . .	13
4	Newton's interactive method flowchart. . . . .	15
5	Unsteady base flow validation. . . . .	16
6	Velocity (left) and viscosity (right) profiles for Newtonian fluid in two different instants ( $t=0$ and $t=0.5T$ ) for $Wm=15$ , $Re=2000$ and $A=1$ . . . . .	23
7	Velocity and its corresponding derivative profiles for $t=0.5T$ Newtonian fluid with $Wm=15$ , $Re=2000$ and $A=1$ . . . . .	24
8	Convergence error for $\lambda=0.5$ and $\mu_\infty=0.0616$ , using equispaced nodes in finite elements with stencil 7. . . . .	24
9	Minimum radial nodes ( $N_{min}$ ) required to fulfill viscosity convergence for different $\lambda$ and $\mu_\infty$ values. . . . .	25
10	Viscosity profiles for different $\lambda$ with each respective $N_{min}$ required for a good shape definition. . . . .	26
11	Blood steady laminar velocity and viscosity profiles. . . . .	27
12	Base flow velocity and viscosity profiles for fixed $\mu_\infty=0.2$ , $n_c=0.35$ , $a=2$ , $Re=2000$ and changing $\lambda$ . . . . .	28
13	Base flow velocity and viscosity profiles for fixed $\lambda=5$ , $n_c=0.35$ , $a=2$ , $Re=2000$ and changing $\mu_\infty$ . . . . .	28
14	Velocity and viscosity profiles for $\lambda=5$ , $Re=2000$ , $Wo=15$ and changing $\mu_\infty$ for different times. Red dashed lines correspond to Newtonian case, blue and green to non-Newtonian case with $\mu_\infty=0.2$ and $\mu_\infty=0.0616$ respectively. . . . .	29
15	Velocity and viscosity profiles for $\mu_\infty=0.0616$ , $Re=2000$ , $Wo=15$ and changing $\lambda$ for different times. Red dashed lines correspond to Newtonian case; blue, green and pink to non-Newtonian case with $\lambda=5$ , $\lambda=20$ and $\lambda=200$ respectively. . . . .	30
16	Velocity and viscosity profiles for $\lambda=5$ , $Re=2000$ , $\mu_\infty=0.2$ and changing $Wo$ for different times. Red dashed lines correspond to Newtonian case; blue, green and pink to non-Newtonian case with $Wo=15$ , $Wo=12.5$ and $Wo=10$ respectively. . . . .	31
17	$m=0,1,2...$ Pulsatile base flow Descending Aorta velocity profiles for different instants. $\lambda=242.2631$ , $\mu_\infty=0.0616$ and $Wo=15$ . Red dashed and blue lines correspond to Newtonian fluid and Desc. Aorta respectively. . . . .	31
18	$m=0,1,2...$ Pulsatile base flow Left Carotid Artery velocity profiles for different instants. $\lambda=722.4477$ , $\mu_\infty=0.0616$ and $Wo=5$ . Red dashed and pink lines correspond to Newtonian fluid and Left Carotid Artery respectively. . . . .	32
19	$m=0,1,2...$ Pulsatile base flow Cerebral Capillaries velocity profiles for different instants. $\lambda=1308.6350$ , $\mu_\infty=0.0616$ and $Wo=2$ . Red dashed and green lines correspond to Newtonian fluid and Cerebral Capillaries respectively. . . . .	32

20	Optimal (a) Newtonian and (b) non-Newtonian perturbations at maximal growth ( $t=1T$ ) on top of non-Newtonian base flow with $\lambda=0.06$ , $Wo=15$ , $Re=2000$ , $A=1$ , $a=2$ , $n_c=0.35$ and $\mu_\infty=0.2$ . . . . .	33
21	Energy plot for (a) Newtonian and (b) non-Newtonian perturbations on top of non-Newtonian base flow with $\lambda=0.06$ , $Wo=15$ , $Re=2000$ , $A=1$ , $a=2$ , $n_c=0.35$ and $\mu_\infty=0.2$ . . . . .	33
22	Upper right plot: Optimal perturbations at maximal energy growth for (a) $\lambda=5$ , $t=0.9T$ and (b) $\lambda=20$ , $t=0.8T$ . Upper left plot: contour of vorticity on a $r-\theta$ cross-section. Bottom plot: time series of the energy growth of the optimal (a) helical $(\alpha,\beta)=(3,1)$ and (b) classic $(\alpha,\beta)=(0,1)$ disturbances at $(Re,A,Wo)=(2000,1,15)$ . . . . .	34
23	Maximal energy growth with respect (a) Reynolds number for different $\lambda$ , (b) fluid's time constant for different $Wo$ and (c) fluid's time constant for different $Wo$ and $\mu_\infty$ . . . . .	35
24	(a) Energy growth of the optimal stream-wise disturbance at $(Re,A,Wo)=(2000,1,15)$ for the desc. aorta $\lambda=242.2631$ and $\mu_\infty=0.0616$ . (b) Time series of kinetic energy contribution of each velocity component for the optimal disturbance. . . . .	36
25	Optimal perturbation at maximal energy growth ( $tf=1.7T$ ) for the descending aorta $\lambda=242.2631$ , $\mu_\infty=0.0616$ . Upper left plot: vorticity contour on a $r-\theta$ cross-section. Bottom plot: time series of the energy growth for two periods. . . . .	36

## List of Tables

1	Carreau and Carreau-Yasuda blood parameters . . . . .	9
2	Steady base flow validation errors . . . . .	13
3	Unsteady base flow validation errors . . . . .	16
4	Cardiovascular sections parameters . . . . .	27
5	Newtonian and non-Newtonian perturbations TGA results. . . . .	33
6	Desc. Aorta parameters and TGA results for the most dangerous perturbation to trigger turbulence transition. . . . .	35

# Abstract

In the last years the major cause of death worldwide has turned out to be because of cardiovascular diseases; for instance, owing to the presence of blood turbulence in our vessels. The problem has already been addressed from simplified points of view that ignore many blood characteristics; consequently, one of the main goals of this project is to take into account the blood shear-thinning effects in an infinite cylindrical pipe and study turbulence transition in such scenario.

With this aim, the first thing to do is a non-Newtonian viscosity models research in order to find the best one to model blood behaviour. After this, an exhaustive base flow study is carried out, for steady and unsteady scenarios, so that finally the Transient Growth Analysis (TGA) provides us with the most dangerous perturbation that could trigger turbulence transition more easily in our veins.

Besides, a parametric study has been performed to take into account a wide range of different possibilities and to be able to highlight more general conclusions.

# 1 Introduction

## 1.1 Motivation and state of the art

In 1883 [16], Reynolds identified the basic problem in the context of flow in a pipe: when and how do high-speed flows undergo transition from laminar state to more complicated scenarios such as puffs, slugs and turbulence? To this day, the problem of the control of fluid turbulence has been under research [18]; often, but not always, to delay its occurrence or mitigate its effects. In addition, it has many practical applications ranging from aeronautics [17] to pipeline engineering [2]. Understanding the phenomenon of turbulence transition initiated by the growth of infinitesimal perturbations is a necessary prerequisite to subsequently find effective transition-delay strategies.

This bachelor's thesis is mainly focused on a more biological background. Cardiovascular diseases represent one, if not the major, cause of death worldwide [20]. With its ever increasing danger in mind, the scientific community is interested on determining its causes for later to be able to prevent them. One of these causes appears to be the presence of turbulence in our cardiovascular system [1]. The only solid understanding regarding transition to turbulence in our arteries or veins comes from the analogy between cardiovascular flow and the elementary Newtonian fluid flow in rigid circular cross-section pipes. It comes with no surprise that, with such a simplified model, many characteristics of blood flow in our flexible vessels are ignored. Most recently, the effects that a pulsating driving flow (instead of a steady driving) has on the transition scenario has been uncovered for a Newtonian fluid [6], [11]. As further steps, it would be interesting to check which are the effects that other previously ignored characteristics of cardiovascular flow have on turbulence transition, specifically shear-thinning effects.

## 1.2 Objectives

As said before, the main intention for this project is to take a step forward in the blood transition to turbulence problem and consider this fluid as non-Newtonian with shear-thinning effects. That is why the main goals of this thesis are:

- First of all, perform a literature research of existing shear thinning fluids models and turbulence transition in order to find the best model to assess this project's problem.
- Secondly, implement a Matlab code to obtain steady/unsteady laminar flows; as well as, implement a further script to perform Transient Growth Analysis.
- Afterwards, an analysis of the flow behaviour and structures in the scope of the linear Navier-Stokes equations is expected to be done in order to find the most dangerous perturbation in each case.
- Finally, the concluding goal would be to perform a parametric study for different shear-thinning conditions, not forgetting the corresponding discussion and conclusions.



## 2 Description of the problem

In order to model pipe flow for non-Newtonian shear thinning fluids an infinite circular cross-section pipe of radius  $\hat{R}$  is considered, where an incompressible fluid flows, the blood (constant fluid density). This last assumption considerably simplifies the equations that must be solved and furthermore, we are dealing with a viscous fluid.

Dimensional parameters are expressed with hat ( $\hat{\cdot}$ ), so the three-dimensional velocity field vector at a given time  $t$  is defined as  $\vec{\hat{u}}(t)=(\hat{u},\hat{v},\hat{w})(t)$ , being  $\hat{u}$ ,  $\hat{v}$  and  $\hat{w}$  the radial, azimuthal and axial velocity components respectively. Therefore, in this whole project cylindrical coordinates are used owing to problem's geometry, with the corresponding derivatives expressed as subscripts. For instance:  $\hat{u}_r$  is the radial derivative of  $\hat{u}$  component and  $\hat{v}_\theta$  is the azimuthal derivative of  $\hat{v}$ .

### 2.1 Non-Newtonian Fluids

The well known scientist Isaac Newton owes his fame to various discoveries and developed theories in mathematics and physics. Among these, he perceived that fluids behave with constant viscosity that could only changes with temperature [19].

However, it was uncovered that stress applied to a fluid plays an important role. Non-Newtonian fluids change their viscosity or flow behaviour under stress, which means that their viscosity is dependent on shear rate; so they are able to get thicker and act more like a solid, or on the other hand, the fluid can get runnier than before. Hence, not all non-Newtonian fluids behave the same way when stress is applied.

To begin with, Newtonian fluids follows a linear relation between shear stress ( $\tau$ ) and shear rate ( $\dot{\gamma}$ ):

$$\tau = \mu \cdot \dot{\gamma} \quad (2.1)$$

so viscosity ( $\mu$ ) is a constant value, no matter how fast the fluid is forced to flow through a pipe or channel.

In contrast, non-Newtonian fluids display a non-linear relation between shear stress and shear rate, as it can be seen in the following figure.

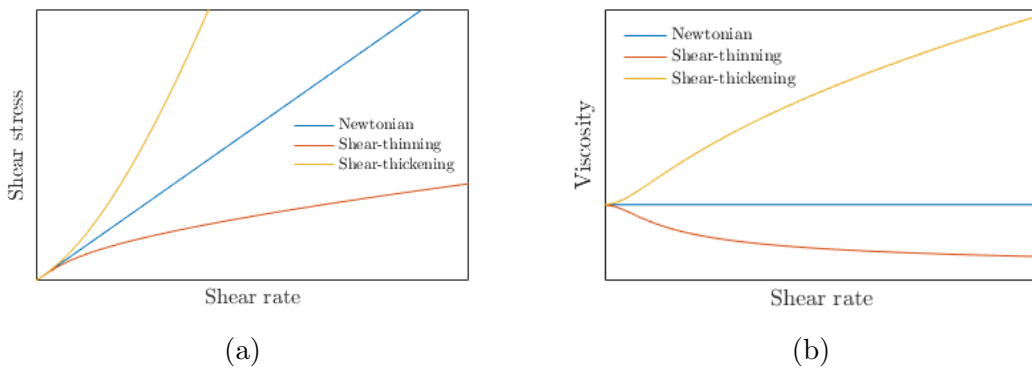


Figure 1: Fluid behaviour according to (a) shear stress, (b) viscosity vs shear rate relation

So a fluid is said to be shear thickening when its viscosity increases as the shear rate does and is said to be shear thinning if its viscosity decreases for higher  $\dot{\gamma}$ . However, this project is mainly focused on shear-thinning fluids, since we want to analyse blood

which behaves as a shear-thinning fluid [21], [8], and surprisingly, not many studies have been carried out concerning transition to turbulence in a pipe for non-Newtonian fluids.

Therefore, it is required to seek for a mathematical law that can approximate the viscosity behaviour and capture the rheological response of blood over a range of flow conditions. After rummaging through the literature, it has been seen that several models are presented for viscous fluid behaviour simulations [3], [9], for instance the well known power law model. However, for a more realistic point of view, it has been decided to use Carreau-Yasuda model in order to simulate the blood viscosity, since it has been found to be the most appropriate model to address the blood problem [13], [14].

### 2.1.1 Carreau-Yasuda model

The model, first proposed by Pierre Carreau, known as Carreau or Carreau-Yasuda, results in a quite realistic representation for shear-thinning/thickening fluids viscosity. It reads as:

$$\mu = \mu_{\infty} + (1 - \mu_{\infty})[1 + (\lambda\dot{\gamma})^a]^{\frac{n_c-1}{a}} \quad (2.2)$$

This expression is already in dimensionless form, such that ' $\dot{\gamma}$ ' stands for the shear rate;  $\mu_{\infty} = \hat{\mu}_{\infty}/\hat{\mu}_0$  is the fluid's viscosity at infinite shear rate, adimensionalized with respect to the zero shear-rate viscosity. When changing this parameter, one can see that a high shear rate values the viscosity profile tends to the desired  $\mu_{\infty}$  value. Then, ' $n_c$ ' stands for the shear-thinning index; so lower ' $n_c$ ' means more shear thinning effect and the viscosity profile would narrow when decreasing it. The term ' $a$ ' describes the shift from zero shear viscosity to the power law zone; such that for higher ' $a$ ' values the shift is flatter, while for lower ' $a$ ' there is more slope. And finally, ' $\lambda$ ' is the fluid's time constant:

$$\lambda = \frac{\hat{\lambda}\hat{U}_{CL}}{\hat{R}} \quad (2.3)$$

being  $\hat{\lambda}$  the dimensional time constant,  $\hat{r}$  and  $\hat{U}_{CL}$  the pipe radius and maximal velocity of the laminar flow respectively. When increasing the fluid's time constant value the viscosity profile narrows; it makes sense as higher time constants force the fluid to reach faster  $\mu_{\infty}$  region.

Besides, for each different fluid all these parameters have an specific value; however, blood is the main fluid in this work, so the upcoming table refers to blood parameters based on which specific model (Carreau or Carreau-Yasuda) is selected [3]. For this reason, Carreau parameters are the ones used in the whole project unless otherwise stated.

	$\hat{\lambda}(s)$	$n_c$	$a$	$\hat{\mu}_0(Pa \cdot s)$	$\hat{\mu}_{\infty} (Pa \cdot s)$
Carreau	3.313	0.35	2	0.056	0.00345
Carreau-Yasuda	1.902	0.22	1.25	0.056	0.00345

Table 1: Carreau and Carreau-Yasuda blood parameters

One can note that Newtonian fluid behaviour is recovered by setting any of the following:  $n_c=1$ ,  $\mu_{\infty}=1$ ,  $\lambda=0$  or  $\dot{\gamma}=0$ .

Furthermore, a visual analysis has been done in order to clearly identify the contrasting viscosity profile regions.

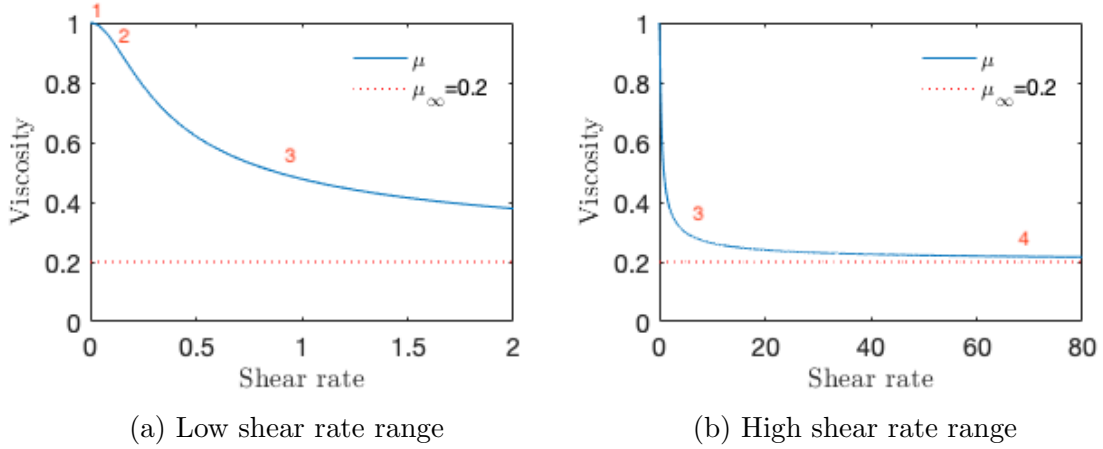


Figure 2: Carreau viscosity profile

1. Zero shear-rate viscosity dominant region. The fluid behaves as a Newtonian one with  $\mu_0$ .
2. Transition region ruled by 'a'.
3. Power-law dominant region.
4. Infinite shear-rate viscosity governing region. The fluid behaves as a Newtonian one with  $\mu_\infty$ .

## 2.2 Governing equations

The governing equations that describe the problem are the continuity and momentum equations complemented with no-slip boundary conditions.

- Continuity equation:

$$\frac{\partial \hat{\rho}}{\partial t} + \nabla(\hat{\rho}\hat{\mathbf{u}}) = 0 \quad (2.4)$$

For incompressible flows it stands that fluid density is constant:  $\hat{\rho} = \text{cnt}$ , which leads to  $\frac{\partial \hat{\rho}}{\partial t} = 0$ , so continuity equation becomes

$$\nabla \hat{\mathbf{u}} = 0 \quad (2.5)$$

- Momentum equation:

$$\hat{\rho} \frac{D\hat{\mathbf{u}}}{Dt} = -\nabla \hat{p} + \nabla \hat{\boldsymbol{\tau}} \quad (2.6)$$

The former equations can be rendered dimensionless using the pipe radius ( $\hat{R}$ ) as length scale, the characteristic velocity ( $\hat{u}_{char}$ ) as velocity scale,  $\hat{r}/\hat{u}_{char}$  as time scale and finally,  $\hat{\rho} \cdot \hat{u}_{char}^2$  as pressure and stress scale.

Two different scenarios should be differentiated:  $\hat{u}_{char} = 2\hat{u}_{bulk}$  for laminar Hagen-Poiseuille flow, while for the unsteady case  $\hat{u}_{char} = 2\hat{u}_s$ , being  $\hat{u}_s$  the bulk velocity time-average.

Consequently, the dimensionless governing equations can be written as:

$$\nabla \mathbf{u} = 0 \quad (2.7)$$

$$\frac{\partial \mathbf{u}}{\partial t} + (\mathbf{u} \nabla) \mathbf{u} = -\nabla p + \frac{1}{Re} \nabla \vec{\tau} \quad (2.8)$$

Reynolds number already appears in (2.8), which measures the ratio between inertial and viscous forces and satisfies the following relation:

$$Re = \frac{\hat{\rho} \hat{u}_{char} \hat{R}}{\hat{\mu}} \quad (2.9)$$

It can also be seen the shear stress tensor ( $\vec{\tau} = \mu \dot{\gamma}$ ) which directly involves viscosity in the main equations, and it shouldn't be overlooked since it require an special treatment as viscosity is not a constant anymore.

Finally, the strain-rate tensor ( $\dot{\gamma}$ ) is defined by:

$$\dot{\gamma} = \nabla \mathbf{u} + (\nabla \mathbf{u})^T = \begin{pmatrix} 2u_r & v_r + \frac{1}{r}(u_\theta - v) & u_z + w_r \\ v_r + \frac{1}{r}(u_\theta - v) & \frac{2}{r}(v_\theta + u) & v_z + \frac{1}{r}w_\theta \\ u_z + w_r & v_z + \frac{1}{r}w_\theta & 2w_z \end{pmatrix} \quad (2.10)$$

Before going into much detail, it must be noted that from now on the equations are expressed in dimensionless form. In any case, the dimensional quantities are written with hat ( $\hat{\phantom{x}}$ ).

### 3 Base Flow

Once familiar with the problem fundamentals, the work can be continued with base flow analysis, which is a crucial and elemental part of this study that helps us to understand how is the pipe flow behaviour in different scenarios and moreover, it is also important for future steps when analyzing transient growth. The importance is more than determining as it will be seen that some laminar flows are closer to develop turbulence transition than others because of their base velocity profiles.

The following subsections particularize the two different situations guiding this project: steady and unsteady/pulsatile base flow.

#### 3.1 Steady Base Flow

Basing on Hagen-Poiseuille flow through an infinite cylindrical pipe, the steady base flow (meaning that it does not change over time) could be considered in this case as one-dimensional, having only an axial component that depends on the radial position, such that:  $\vec{u}_b = w_b(r) \vec{e}_z$ . Furthermore, pressure is driven by a constant gradient ' $G_p$ ', satisfying also a constant rate flow constraint corresponding to  $Q=1$ . Hence, the unknown variables correspond to pressure gradient and axial velocity  $\begin{pmatrix} G_p \\ w_b \end{pmatrix}$ .

Substituting this base flow properties in the momentum equation 2.8, it can be seen that radial and azimuthal components banish and axial direction equation stands as:

$$0 = G_p + \frac{1}{Re} \frac{1}{r} \frac{d}{dr} \left( r \mu_b \frac{dw_b}{dr} \right) \quad (3.1)$$

Where the viscosity base flow term writes as:

$$\mu_b = \mu_\infty + (1 - \mu_\infty) \left[ 1 + \left( \lambda \frac{dw_b}{dr} \right)^a \right]^{\frac{n_c - 1}{a}} = \mu_\infty + \mu_p \quad (3.2)$$

As stated before, 3.1 is complemented with no-slip boundary conditions at the wall and moreover, with the aim of solving this equation, the radial coordinate must be discretized; in this case, by means of Chebyshev nodes (see section 3.1.1). Additionally, since there is a non-linear term in 3.1, the iterative Newton's Raphson method is the one used to converge to the desired solution (see section 3.1.2).

Doing slightly further work, 3.1 could be expressed as the sum of a linear and non-linear terms:

$$0 = ReG_p + \mu_\infty \left( \frac{1}{r} \frac{\partial}{\partial r} + \frac{\partial^2}{\partial r^2} \right) w_b + \left( \frac{1}{r} + \frac{\partial}{\partial r} \right) \left( \mu_p \frac{\partial w_b}{\partial r} \right) \quad (3.3)$$

$$0 = ReG_p + Lw_b + CNL \cdot NL \quad (3.4)$$

Displaying the equation this way allows easier computation of the corresponding Jacobian, which is strictly needed to evaluate each Newton iteration. So recalling that ' $G_p$ ' and ' $w_b$ ' are the variables, the Jacobian reads as:

$$J = \begin{pmatrix} 0 & 2 \cdot r \cdot wei \\ Re & L + CNL \cdot \left( \mu_p \frac{\partial}{\partial r} + \frac{\partial w_b}{\partial r} \frac{\partial \mu_p}{\partial w_b} \right) \end{pmatrix} \quad (3.5)$$

where first row corresponds to the constraint  $Q=1$ , with  $wei$  being the integration Clenshaw-Curtis weights.

Steady Matlab code validation has been successfully done comparing the obtained results with those already published in López-Carranza paper [15]. For this purpose, base velocity profiles with the same parameters as the ones in [15] have been computed. The following figures show the velocity profile for the Newtonian and non-Newtonian scenarios with  $n_c=1$  and  $n_c=0.5$  respectively;  $\lambda=30$ ,  $a=2$ ,  $Re=1000$  and  $\mu_\infty=0.002$  are common in both cases.

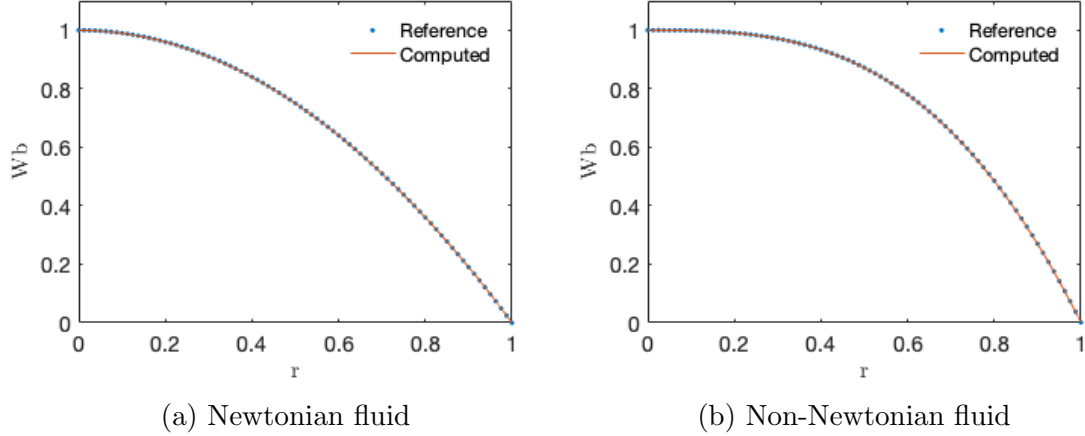


Figure 3: Steady base flow validation

What is more, the mean square error has been computed for both situations, such that for  $N=500$  (number of radial discretized points):

	Newtonian	Non-Newtonian
MSE $(m/s)^2$	$6.87 \cdot 10^{-7}$	$6.80 \cdot 10^{-7}$

Table 2: Steady base flow validation errors

### 3.1.1 Chebyshev discretization

The discrete rendering of the problem's geometry is a crucial key when solving Computational Fluid Dynamics (CFD) tasks, owing to the fact that the designated points or cells where the flow properties are solved have a significant impact on the convergence, solution accuracy and required time. Therefore, it is interesting to be able to find a suitable balance between grid density, skewness, boundary layers, etc. to obtain pleasant solutions.

Due to the accuracy they offer, we use Chebyshev polynomials in the radial direction. The first idea someone might have is to use equispaced points to generate the grid; however, it turns out to be catastrophically bad in general. Hence, when doing approximations in  $N$  equally spaced points, it not only fail to converge for large  $N$ , but the approximation get worse at a rate that may be as great as  $2^N$  [22].

Thus, it can be deduced that the right idea would be to use unevenly spaced points. Different sets of points are efficient, nevertheless they all share the following density

property as  $N \rightarrow \infty$ :

$$density \sim \frac{N}{\pi\sqrt{1-x^2}} \quad (3.6)$$

In this thesis the so-called *Chebyshev points* set, which satisfy 3.6, are used:

$$x_j = \cos\left(\frac{j\pi}{N}\right), \quad j = 0, 1, 2, \dots, N. \quad (3.7)$$

Geometrically, these points can be visualized as the projections on  $[-1,1]$  of equispaced points on the upper half of a unit circle; so accordingly, they appear to be clustered towards the boundaries. The effect of using clustered points on the accuracy of the approach is terrific compared with equispaced grids, for spectral methods based on polynomials.

Furthermore, these points can be used to construct the Chebyshev differentiation matrices, as skilfully explained in "Spectral Methods in Matlab" [22], which will be certainly useful along the whole project.

### 3.1.2 Iterative Newton's method

The discretized equations are solved iteratively using the Newton's method, also known as Newton-Raphson method. It is a root-finding based algorithm; thus, the system is first evaluated on a set of initial guessed radial points (corresponding to the Newtonian base flow velocity profile) that together with the corresponding jacobian, allows the computation of the next better approximated result. Moreover, the handmade implemented Newton code adds a new constraint: the following iteration is only computed when the solution is closer to the desired one, is to say, when the solution is closer to zero. If not, there is a step size parameter ( $ss$ ) that helps to fulfill this requirement.

$$x_{k+1} = x_k - ss \frac{f(x_k)}{f'(x_k)} \quad (3.8)$$

Therefore, in case the new solution is not closer to the desired one, the step size parameter is taken to be:  $ss=ss/2$ . Once the requirement is fulfilled,  $ss$  is settled again to  $ss=1$ .

So the iterative process is repeated until the error is reduced up to  $10^{-12}$ ; once this is reached, it can be considered that the result has converged and then it changes to the next step, taking as initial velocity guess the previous converged profile. Moreover, the Newton's method also stops if  $k$  (number of iterations) is bigger than 200 or if  $ss$  becomes very small without a converged solution.

Next figure display the flowchart which describe this Newton's iterative method.

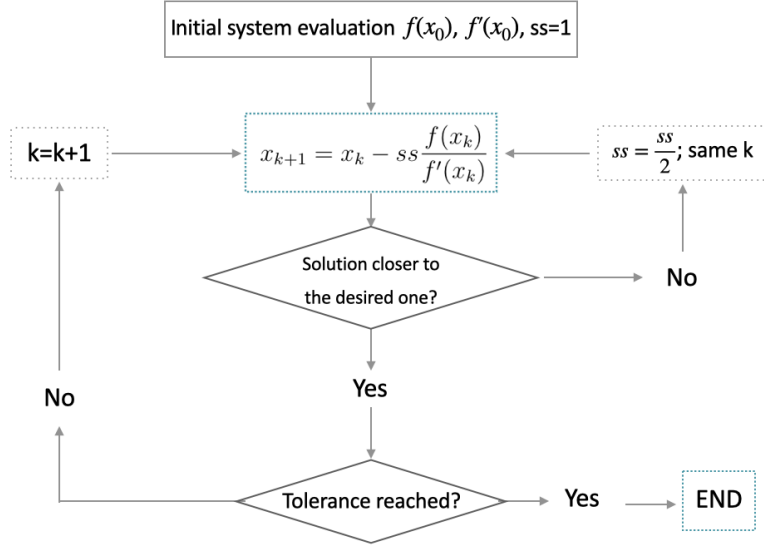


Figure 4: Newton's iterative method flowchart.

### 3.2 Unsteady Base Flow

Unsteady base flow corresponds to the scenario when the laminar flow changes over time; specifically, in this project a pulsatile model has been chosen such that the imposed pressure gradient constraint meets the following flow rate relation,

$Q = u_m - A \cos(wt)$ , being ' $u_m$ ' the mean velocity; 'A' and 'w' the amplitude and angular frequency of the pulsation respectively. Transition to turbulence in this case also depends on a new parameter called Womersley number  $Wo$ , which represents the relation between pulsation frequency ( $f$ ) and viscous effects:

$$Wo = \frac{D}{2} \sqrt{\frac{2\pi f}{\nu}} \quad (3.9)$$

So now, since the problem is time dependent, an additional term corresponding to the laminar velocity time derivative must be added to the equation 3.1.

$$Re \frac{\partial w_b}{\partial t} = Re G_p + L w_b + CNL \cdot NL \quad (3.10)$$

Time discretization has been chosen to be carried out by a second order backward differentiation formula (BDF2), which is an implicit method for numerical integration. For a given function and time, this multistep method approximates the respective derivative using previously computed values. Hence, the corresponding BDF2 formula for the problem  $y' = f(t, y)$  would be:

$$y_{n+2} - \frac{4}{3}y_{n+1} + \frac{1}{3}y_n = \frac{2}{3}h f(t_{n+2}, y_{n+2}) \quad (3.11)$$

where h denotes the integration step size.

Bearing this in mind, as well as recalling that ' $G_p$ ' and ' $w_b$ ' are the unknown variables, the unsteady flow Jacobian reads as:

$$J = \begin{pmatrix} 0 & 2 \cdot r \cdot wei \\ -\frac{2}{3}dt Re & Re - \frac{2}{3}dt [L + CNL \cdot (\mu_p \frac{\partial}{\partial r} + \frac{\partial w_b}{\partial r} \frac{\partial \mu_p}{\partial w_b})] \end{pmatrix} \quad (3.12)$$



Finally, the pulsatile Matlab code validation has also been successfully done for the Newtonian case, such that the computed profile has been validated with Sexl-Womersley exact analytical solution.

For instance, the following plots correspond to a Newtonian fluid with parameters:  $A=1$ ,  $Wo=15$  and  $Re=2000$  in two different times.

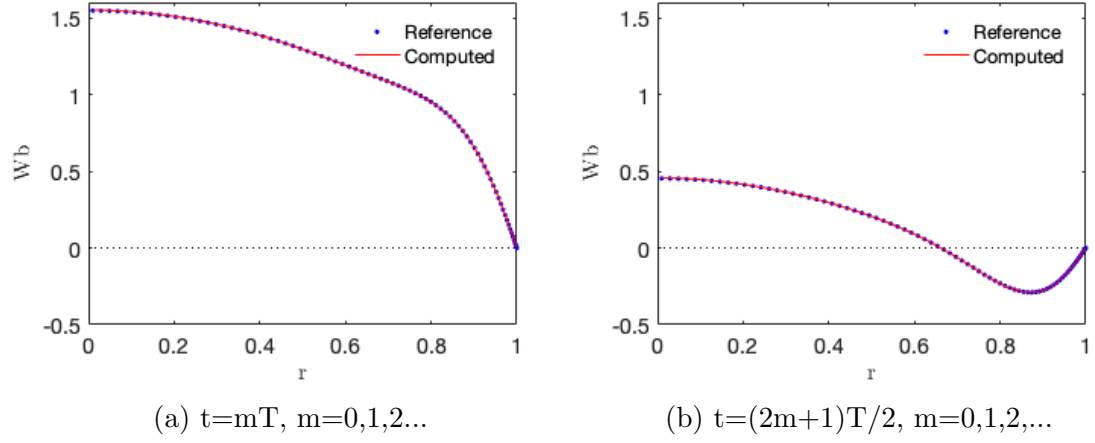


Figure 5: Unsteady base flow validation.

Once again, the mean square error corresponding to both different times has been computed; so taking into account that  $m=0,1,2,\dots$  the respective mean square errors for  $N=80$  are:

	$t=mT$	$t=(2m+1)T/2$
MSE $(m/s)^2$	$1.46 \cdot 10^{-6}$	$9.95 \cdot 10^{-7}$

Table 3: Unsteady base flow validation errors

## 4 Transient Growth Analysis (TGA)

In this section, the transient evolution of perturbations on top of the previous base flows is considered. So first of all, the corresponding linearization of the Navier-Stokes equations will be seen, followed by a brief description of the theoretical fundamentals and as a last section, also a short and concise explanation of the method used to implement TGA.

### 4.1 Disturbance and linearized Navier-Stokes equations

”Hydrodynamic stability theory is concerned with the response of a laminar flow to a disturbance of small or moderate amplitude” [10]. Generally, disturbances are considered infinitesimal so that further simplifications could be justified; for instance, the governing linear equation of the disturbance evolution is yearned. However, nonlinear effects turn out to be significant once the disturbance velocities grow above the base flow; at this point, the linear equations are not completely precise to predict the disturbance evolution. Despite the fact that the linear equations have a limited region of validity they are of great importance for physical growth mechanisms detection, as much as dominant disturbance types identification.

Thus, the base flow is initially perturbed by an infinitesimal disturbance  $(\mathbf{u}, p)$  such that:  $\mathbf{U} = \vec{u}_b + \epsilon \mathbf{u}$  and  $P = p_b + \epsilon p$ , where variables  $'\vec{u}_b'$  and  $'p_b'$  correspond to the base flow. The governing time evolution equation of the disturbance is obtained by introducing these perturbations to the momentum equation, keeping the lowest order (linear) terms in  $\epsilon$  and setting quadratic terms to zero:

$$\frac{\partial \mathbf{u}}{\partial t} + (\vec{u}_b \nabla) \mathbf{u} + (\mathbf{u} \nabla) \vec{u}_b = -\nabla p + \frac{1}{Re} \nabla (\vec{\tau}_{u_b + u} - \vec{\tau}_{u_b}) \quad (4.1a)$$

$$\nabla \mathbf{u} = 0 \quad (4.1b)$$

Regarding the solution of 4.1, two main questions have to be considered. The first one states: is there a solution that grows boundless? If so, the base flow  $\vec{u}_b$  is linearly unstable. The second question stands for: given a linearly stable base flow, is there any bounded solution that manifest large transient growth before the inevitable decay? In these cases, it can be considered that the base flow is linearly stable; however, susceptibility to nonlinear instability is present, as well as some local regions of convective instability. Hence, when answering both questions, it is wished to find the perturbation that produces optimal growth.

As noted before, an infinitesimal disturbance is applied; therefore, the term standing for the shear stress tensor  $\vec{\tau}' = \vec{\tau}_{u_b + u} - \vec{\tau}_{u_b}$  has to be linearized around the base flow  $(\vec{u}_b, p_b)$ . To this purpose, detailed analysis of each term is performed, starting with viscosity term  $\mu(\vec{u}_b + \mathbf{u})$ , which is linearized by a Taylor expansion. It should be called up that  $\vec{\tau}(\vec{u}) = \mu(\vec{u}) \dot{\gamma}(\vec{u})$ , besides taking into account that  $\dot{\gamma}$  is a linear term so:  $\dot{\gamma}(\vec{u}_b + \mathbf{u}) = \dot{\gamma}(\vec{u}_b) + \dot{\gamma}(\mathbf{u})$ .

$$\mu(\vec{u}_b + \mathbf{u}) = \mu(\dot{\gamma}_b + \dot{\gamma}(\mathbf{u})) = \mu_b + \frac{1}{2} \frac{\partial \mu}{\partial \dot{\gamma}_{ij}} \Big|_b : \dot{\gamma}_{ij}(\mathbf{u}) = \mu_b + \frac{\partial \mu}{\partial \dot{\gamma}_{rz}} \Big|_b \left( \frac{\partial w}{\partial r} + \frac{\partial u}{\partial z} \right) \quad (4.2)$$

Introducing 4.2 in  $\vec{\tau}'$ , as well as neglecting infinitesimal terms:

$$\vec{\tau}' = \vec{\tau}_{u_b+u} - \vec{\tau}_{u_b} = \mu(\vec{u}_b + \mathbf{u}) [\dot{\gamma}(\vec{u}_b) + \dot{\gamma}(\mathbf{u})] - \mu_b \dot{\gamma}_b = \mu_b \dot{\gamma}(\mathbf{u}) + \left. \frac{\partial \mu}{\partial \dot{\gamma}_{rz}} \right|_b \left( \frac{\partial w}{\partial r} + \frac{\partial u}{\partial z} \right) \dot{\gamma}_b \quad (4.3)$$

$$\left. \frac{\partial \mu}{\partial \dot{\gamma}_{rz}} \right|_b = (1 - \mu_\infty)(n_c - 1) \lambda^a \left[ 1 + \lambda^a \left| \frac{\partial w_b}{\partial r} \right|^a \right]^{\frac{n_c-1}{a}-1} \left| \frac{\partial w_b}{\partial r} \right|^{a-1} \frac{\partial w_b}{\partial r} \quad (4.4)$$

Once the disturbance shear stress tensor has been worked out, next step would be applying the divergence at each term:

$$\nabla(\mu_b \dot{\gamma}(\mathbf{u})) = \mu_b \Delta \mathbf{u} + \left( \frac{\partial \mu_b}{\partial r}, 0, 0 \right) \dot{\gamma}(\mathbf{u}) = \mu_b \Delta \mathbf{u} + \begin{pmatrix} 2u_r \frac{\partial \mu_b}{\partial r} \\ [v_r + \frac{1}{r}(u_\theta - v)] \frac{\partial \mu_b}{\partial r} \\ [u_z + w_r] \frac{\partial \mu_b}{\partial r} \end{pmatrix} \quad (4.5)$$

$$\begin{aligned} \nabla \left( \left. \frac{\partial \mu}{\partial \dot{\gamma}_{rz}} \right|_b (w_r + u_z) \dot{\gamma}_b \right) &= \nabla \begin{pmatrix} 0 & 0 & \left[ \left. \frac{\partial \mu}{\partial \dot{\gamma}_{rz}} \right|_b (w_r + u_z) \right] \frac{\partial w_b}{\partial r} \\ 0 & 0 & 0 \\ \left[ \left. \frac{\partial \mu}{\partial \dot{\gamma}_{rz}} \right|_b (w_r + u_z) \right] \frac{\partial w_b}{\partial r} & 0 & 0 \end{pmatrix} = \\ &= \begin{pmatrix} \frac{\partial}{\partial z} \left[ \left. \frac{\partial \mu}{\partial \dot{\gamma}_{rz}} \right|_b (w_r + u_z) \right] \frac{\partial w_b}{\partial r} \\ 0 \\ \frac{\partial}{\partial r} \left[ \left. \frac{\partial \mu}{\partial \dot{\gamma}_{rz}} \right|_b (w_r + u_z) \right] \frac{\partial w_b}{\partial r} \end{pmatrix} \end{aligned} \quad (4.6)$$

In accordance, shear stress tensor divergence would write as:

$$\nabla \vec{\tau}' = \mu_b \Delta \mathbf{u} + \begin{pmatrix} 2u_r \frac{\partial \mu_b}{\partial r} + \left. \frac{\partial \mu}{\partial \dot{\gamma}_{rz}} \right|_b (w_{rz} + u_{zz}) \frac{\partial w_b}{\partial r} \\ [v_r + \frac{1}{r}(u_\theta - v)] \frac{\partial \mu_b}{\partial r} \\ [u_z + w_r] \frac{\partial \mu_b}{\partial r} + [A1] \frac{\partial w_b}{\partial r} + \left. \frac{\partial \mu}{\partial \dot{\gamma}_{rz}} \right|_b (w_r + u_z) \frac{\partial^2 w_b}{\partial r^2} \end{pmatrix} \quad (4.7)$$

$$A1 = \frac{\partial}{\partial r} \left( \left. \frac{\partial \mu}{\partial \dot{\gamma}_{rz}} \right|_b \right) (w_r + u_z) + \left. \frac{\partial \mu}{\partial \dot{\gamma}_{rz}} \right|_b (w_{rr} + u_{zr}) \quad (4.8)$$

Finally, after having developed the other terms from 4.1a, plus splitting in velocity components, the linearized Navier-Stokes equations (LNSE) for an infinitesimal disturbance are obtained:

$$u_t + w_b u_z = -p_r + \frac{1}{Re} \left[ \mu_b \left( \Delta u - \frac{u}{r^2} - \frac{2}{r^2} v_\theta \right) + 2u_r \frac{\partial \mu_b}{\partial r} + \left. \frac{\partial \mu}{\partial \dot{\gamma}_{rz}} \right|_b (w_{rz} + u_{zz}) \frac{\partial w_b}{\partial r} \right] \quad (4.9)$$

$$v_t + w_b v_z = -\frac{1}{r} p_\theta + \frac{1}{Re} \left[ \mu_b \left( \Delta v - \frac{v}{r^2} + \frac{2}{r^2} u_\theta \right) + \left( v_r + \frac{1}{r} [u_\theta - v] \right) \frac{\partial \mu_b}{\partial r} \right] \quad (4.10)$$

$$w_t + u \frac{\partial w_b}{\partial r} + w_b w_z = -p_z + \frac{1}{Re} \left[ \mu_b \Delta w + (w_r + u_z) \frac{\partial \mu_b}{\partial r} + A1 \frac{\partial w_b}{\partial r} + \frac{\partial \mu}{\partial \gamma_{rz}} \Big|_b (w_r + u_z) \frac{\partial^2 w_b}{\partial r^2} \right] \quad (4.11)$$

Equations 4.1b, 4.9, 4.10 and 4.11 are linear, periodic in  $\theta$  and unbounded in  $z$  (due to the cylindrical domain); so moreover, as introduced in Meseguer et al. paper [4], all solutions to these equations can be expressed as superposition of complex Fourier modes of the form

$$\mathbf{u}(r, \theta, z, t) = e^{i(\beta\theta + \alpha z)} \mathbf{u}(r, t); \quad p(r, \theta, z, t) = e^{i(\beta\theta + \alpha z)} p(r, t) \quad (4.12)$$

where  $\beta \in Z$  and  $\alpha \in R$  are the azimuthal and axial wavenumbers respectively. Introducing 4.12 into 4.9, 4.10 and 4.11 gives simplified equations that are easier to implement in Matlab.

## 4.2 Theoretical fundamentals

### 4.2.1 Linear stability

As distinctively explained in [5], a linear evolution operator  $\Lambda(t)$  could be defined to represent the disturbance evolution forward in time:

$$\mathbf{u}(t) = \Lambda \mathbf{u}(0) \quad (4.13)$$

Through this forward evolution operator it is easy to access the linear stability of the base flow. Two different scenarios could be distinguished: for a steady base flow, LNSE are autonomous with eigenmode solutions of the form  $\mathbf{u}(\mathbf{x}, t) = \exp(\lambda_j t) \vec{u}_j(\mathbf{x}) + C$ ; for an unsteady periodic base flow (with period  $T$ ), LNSE becomes a Floquet problem with solutions of the form  $\mathbf{u}(\mathbf{x}, t) = \exp(\lambda_j t) \vec{u}_j(\mathbf{x}, t) + C$ , where  $\vec{u}_j(\mathbf{x}, t+T) = \vec{u}_j(\mathbf{x}, t)$ .

In either case, an eigenvalue problem in terms of the operator  $\Lambda(T)$  is obtained once time  $t$  is settled to a value  $t_f$ .

$$\Lambda(t_f) \vec{u}_j = \eta_j \vec{u}_j, \quad \eta_j = \exp(\lambda_j t_f) \quad (4.14)$$

The dominant eigenvalues of  $\Lambda(t_f)$ ,  $\eta_j$  of the largest modulus, are used to determine the classical linear stability of the base flow.

- If any  $\eta_j$  comply with  $|\eta_j| > 1$ , there exist exponentially growing solutions and the base flow is linearly unstable.
- If every  $\eta_j$  comply with  $|\eta_j| < 1$ , all solutions decay to zero and the base flow is linearly stable.
- $|\eta_j| = 1$  is a sign of bifurcation point

### 4.2.2 Transient Growth assessment

In particular, what is about to be studied is the second main question introduced in the linearized equations section (4.1): given a linearly stable base flow, is there any bounded solution that manifest large transient growth before the inevitable decay?

Perturbations will exhibit substantial transient response due to regions of localized convective instability, as [5] corroborate. The asymmetry of the convective terms in the Navier-Stokes equations leads to non-orthogonal eigenmodes; the aforementioned affects the form of the dynamics of interest, which in fact won't be an exponential function of time multiplying a fixed modal shape. Hereafter, transient growth analysis is going to be the way to quantify such dynamics.

Transient growth is assessed as the normalized perturbation energy at time  $\tau$  to its initial energy. Considering normalized initial perturbations, a new parameter known as energy growth (G), the one that is optimized in this method, is defined as the ratio between the total perturbation kinetic energy at time  $\tau$  and  $t_0$ :

$$G(\tau) = \frac{E(\tau)}{E(0)} = \|\mathbf{u}(\tau)\|^2 = (\mathbf{u}(\tau), \mathbf{u}(\tau)) \quad (4.15)$$

Where the standard  $L_2$  inner product is present:

$$(\mathbf{u}, \mathbf{v}) = \int_{\Omega} \mathbf{u} \mathbf{v} dv \quad (4.16)$$

Introducing 4.13 into 4.15 leads to:

$$\frac{E(\tau)}{E(0)} = (\Lambda(\tau)\mathbf{u}(0), \Lambda(\tau)\mathbf{u}(0)) = (\mathbf{u}(0), \Lambda^*(\tau)\Lambda(\tau)\mathbf{u}(0)) \quad (4.17)$$

Being  $\Lambda^*(\tau)$  the adjoint evolution operator of  $\Lambda(\tau)$ . Henceforth, the main question should be remodeled: which is the disturbance that leads to maximal growth? For the stability problem, the greatest importance falls on the dominant eigenvalues, since they stand for the "worst case scenario", so the eigenfunctions corresponding to the dominant eigenvalues ( $\lambda_j$ ) of  $\Lambda^*(\tau)\Lambda(\tau)$  will describe the largest possible growth.

$$G_{max}(\tau) = \max \frac{E(\tau)}{E(0)} = \max \lambda_j \quad (4.18)$$

### 4.3 Improved Projection Scheme (IPS)

In this subsection, the numerical method implemented to compute transient growth is explicitly detailed. This specific scheme has been chosen since its efficiency and outstanding temporal behaviour for sufficiently large time integration are a key feature to capture three-dimensional simulations of unsteady flows.

One of the major problems when solving the incompressible Navier-Stokes equations concerns the coupling of pressure and velocity to satisfy the incompressibility constraint. Indeed, the pressure gradient varies for time-dependent flows while preserving its boundary value fixed, held at its initial value, during time integration. To assess this, a pressure predictor is introduced to provide a suitable pressure field with a divergence free velocity. As it is also highlighted in [12], the temporal scheme's accuracy order used is kept for the pressure and velocity when using this algorithm.

#### 4.3.1 IPS for Newtonian fluids

Considering an incompressible Newtonian fluid, the respective governing Navier-Stokes equations:

$$\frac{\partial \mathbf{u}}{\partial t} + (\mathbf{u} \nabla) \mathbf{u} = -\nabla p + \frac{1}{Re} \Delta \mathbf{u} \quad (4.19)$$

Distinguishing the linear and non-linear terms, the former equation could be expressed as:

$$\frac{\partial \mathbf{u}}{\partial t} + NL(\mathbf{u}) = -\nabla p + \frac{1}{Re}L(\mathbf{u}) \quad (4.20)$$

$$\nabla \mathbf{u} = 0 \quad (4.21)$$

Applying divergence on the Navier-Stokes, plus taking into account that velocity is divergence free ( $\nabla \mathbf{u}=0$ ), the Poisson equation is derived:

$$\nabla NSE \rightarrow \nabla\left(\frac{\partial \mathbf{u}}{\partial t}\right) + \nabla NL(\mathbf{u}) = -\Delta p + \frac{1}{Re}\nabla L(\mathbf{u}) \rightarrow \nabla^2 p = -\nabla NL(\mathbf{u}) \quad (4.22)$$

However, a consistent boundary condition is required to solve the Poisson equation, which can be derived from 4.20 and 4.21:

$$\frac{\partial p}{\partial \hat{n}} = \hat{n} \left[ -\frac{\partial \mathbf{u}}{\partial t} - NL(\mathbf{u}) + \frac{1}{Re}L(\mathbf{u}) \right] \quad (4.23)$$

As remarkably mentioned in [12], the time accuracy of the global solution is directly dependent on the treatment of these pressure boundary conditions. So now, it should be remembered that spatial approximation is accomplished by Chebyshev discretization and the temporal scheme obey an Adams-Bashforth and BDF combination of second-order accuracy, such that equation 4.20 reads as:

$$\frac{3\mathbf{u}^{n+1} - 4\mathbf{u}^n + \mathbf{u}^{n-1}}{2\Delta t} + 2NL(\mathbf{u}^n) - NL(\mathbf{u}^{n-1}) = -\nabla p^{n+1} + \frac{1}{Re}\Delta(\mathbf{u}^{n+1}) \quad (4.24)$$

By such means, the main steps to follow in order to get the perturbation components proceed as:

(i) Pressure  $p^{n+1}$  prediction:

$$\Delta p^{n+1} = -\nabla (2NL(\mathbf{u}^n) - NL(\mathbf{u}^{n-1})) \quad (4.25)$$

$$\left. \frac{\partial p^{n+1}}{\partial \hat{n}} \right|_{wall} = \hat{n} \left[ \frac{-3\mathbf{u}_{bc}^{n+1} + 4\mathbf{u}^n - \mathbf{u}^{n-1}}{2\Delta t} - 2NL(\mathbf{u}^n) + NL(\mathbf{u}^{n-1}) + \frac{1}{Re}(2L(\mathbf{u}^n) - L(\mathbf{u}^{n-1})) \right] \quad (4.26)$$

Where  $\mathbf{u}_{bc}$  stands for the velocity boundary conditions.

(ii) Velocity  $\mathbf{u}^*$  prediction from the momentum equation, including the new pressure field and with boundary condition  $\mathbf{u}^*=\mathbf{u}_{bc}^{n+1}$ .

$$\frac{3\mathbf{u}^* - 4\mathbf{u}^n + \mathbf{u}^{n-1}}{2\Delta t} + 2NL(\mathbf{u}^n) - NL(\mathbf{u}^{n-1}) = -\nabla p^{n+1} + \frac{1}{Re}\Delta(\mathbf{u}^*) \quad (4.27)$$

(iii) Intermediate step. An intermediate variable  $\phi$ , defined as  $\phi = \frac{2\Delta t}{3}(p^{*(n+1)} - p^{n+1})$ , is introduced when the final divergence-free velocity field is explicitly evaluated, such that:

$$\frac{3\mathbf{u}^{n+1} - 3\mathbf{u}^*}{2\Delta t} = -\nabla(p^{*(n+1)} - p^{n+1}) \quad (4.28)$$

So taking the divergence of the former equation, a new Poisson equation for  $\phi$  arise

$$\Delta \phi = \nabla \mathbf{u}^* \quad (4.29)$$

which can be solved together with the consistent Neumann boundary condition, as a means to get  $\phi$ :

$$\frac{\partial \phi}{\partial \hat{n}} = 0 \quad (4.30)$$

(iv) As a last step, update the corrected velocity field:

$$\mathbf{u}^{n+1} = \mathbf{u}^* - \nabla \phi \quad (4.31)$$

Finally, this scheme is applied to the linear Navier Stokes equations for a Newtonian fluid and their corresponding adjoint to integrate forward and backward in time iteratively, until a Krylov space is built and from which is possible to obtain the optimal perturbation for each specific  $Wm$ ,  $Re$ ,  $\lambda$  and  $A$  scenario.

It has to be noted that TGA code was already implemented in [6] study; new contribution appears in the next section where the non-Newtonian terms will be taken into account to compute Transient Growth Analysis.

#### 4.3.2 IPS for non-Newtonian fluids

In this section, IPS for an incompressible non-Newtonian fluid is introduced. For this purpose, few line code modifications have been done in order to insert the non-Newtonian contribution to the model.

Therefore, the equations leading this scenario are nothing more than the linearized Navier Stokes equations for a non-Newtonian fluid presented in section 4.1, corresponding to equations 4.9, 4.10 and 4.11, which could be expressed in the compact form (similar to eq. 4.20):

$$\frac{\partial \mathbf{u}}{\partial t} + NL(\mathbf{u}) = -\nabla p + \frac{1}{Re} [\mu_b L(\mathbf{u}) + NN(\mathbf{u})] \quad (4.32)$$

What is more,  $NN$  term can be treated just like  $NL$ . Hence,  $NL'(\mathbf{u}) = NL(\mathbf{u}) - \frac{1}{Re} NN(\mathbf{u})$  and:

$$\frac{\partial \mathbf{u}}{\partial t} + NL'(\mathbf{u}) = -\nabla p + \frac{1}{Re} \mu_b L(\mathbf{u}) \quad (4.33)$$

Applying again divergence on the former equation, a different expression than the Poisson equation is obtained; since as quickly seen, the appearance of the viscosity ( $\mu_b$ ) prevents the linear term from vanish.

$$\nabla \left( \frac{\partial \mathbf{u}}{\partial t} \right) + \nabla NL'(\mathbf{u}) = -\Delta p + \frac{1}{Re} \nabla (\mu_b L(\mathbf{u})) \rightarrow \nabla^2 p = -\nabla NL(\mathbf{u}) + \frac{1}{Re} L(\mathbf{u}) \nabla \mu_b \quad (4.34)$$

The consistent boundary condition required to solve the previous equations reads as:

$$\frac{\partial p}{\partial \hat{n}} = \hat{n} \left[ -\frac{\partial \mathbf{u}}{\partial t} - NL'(\mathbf{u}) + \frac{1}{Re} \mu_b L(\mathbf{u}) \right] \quad (4.35)$$

Hereafter, the following discretization treatment keeps the same as the IPS Newtonian case, as well as the four main steps.

## 5 Convergence Analysis

As well argued in section 3.1.1, the discrete rendering of the problem's geometry is a crucial key when solving CFD tasks in view of the fact that convergence and solution accuracy depend on it. During the base flow results analysis, it has been surprising to discover that the viscosity profile is not at all well defined, wiggles appear throughout the whole domain. Hence, the main goal of the following analysis is to determine the minimum number of radial nodes ( $N_{min}$ ) needed to satisfactory capture the viscosity behaviour for different increasing  $\lambda$  values, which is the dimensionless fluid's time constant. Besides, in this convergence analysis Chebyshev nodes are left out for finite differentiation using an equispaced grid of stencil 7.

With the aim of finding  $N_{min}$ , a fixed velocity profile, specifically corresponding to  $t=0.5T$  Searl-Womersley base flow for  $Wo=15$ ,  $Re=2000$  and  $A=1$ , has been chosen to be the one for viscosity computation. It should be noted that any other velocity profile could be valid to carry out this convergence analysis; however, the interest falls on the profiles with more complex shapes. In other words, the interest falls on the ones with maximums/minimums near the pipe wall that would trigger the viscosity rapidly to 1 (because the velocity derivative would be zero), giving way to the appearance of sudden peaks in the viscosity profile.

$$\frac{dW_b}{dr} = 0 \rightarrow \mu = \mu_\infty + (1 - \mu_\infty) \left[ 1 + \lambda^a \cdot \left( \frac{dW_b}{dr} \right)^a \right]^{(n_c-1)/a} \rightarrow \mu = 1 \quad (5.1)$$

Hence, this is the reason why  $t=0.5T$  Searl-Womersley profile is chosen and not  $t=0$  for example. Figure 6 shows the appearance of the mentioned peak due to the minimum in the velocity profile between  $0.8 < r < 1$ . Moreover, the peak is not well defined and the purpose of this study falls on finding the minimum radial nodes  $N_{min}$  such that this crest is well delineated. Figure 7 displays the chosen velocity profile with its corresponding radial derivative, which remains the same throughout the analysis.

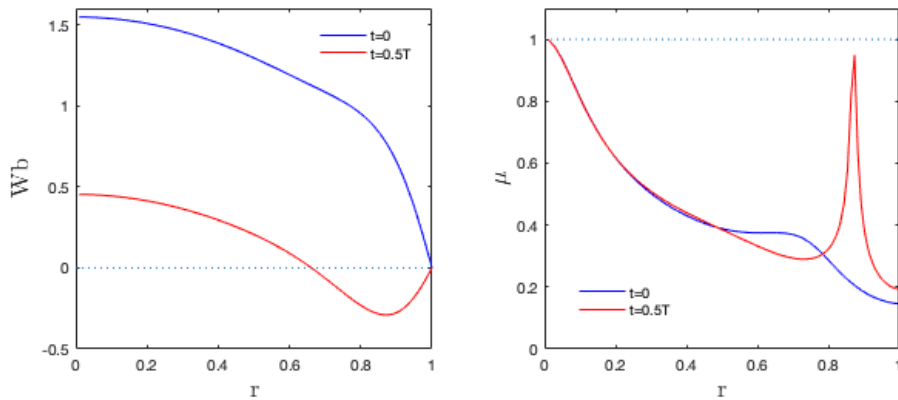


Figure 6: Velocity (left) and viscosity (right) profiles for Newtonian fluid in two different instants ( $t=0$  and  $t=0.5T$ ) for  $Wm=15$ ,  $Re=2000$  and  $A=1$ .



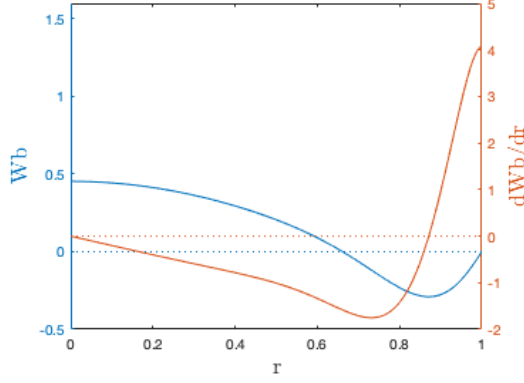


Figure 7: Velocity and its corresponding derivative profiles for  $t=0.5T$  Newtonian fluid with  $Wm=15$ ,  $Re=2000$  and  $A=1$ .

So, starting from a fixed low  $\lambda$  value and  $N=80$ , the viscosity profile ( $\mu_b$ ) is computed, from which the term  $C$  (used to assess convergence) can be determined:

$$C(N) = \int_r \mu_b^2(N) dr \quad (5.2)$$

Subsequently, while increasing the radial nodes it is possible to compare the new  $C$  value with the previous one, such that this  $N$  rising procedure is continued until a constraint is fulfilled. In this specific case, the required restriction was for the last four  $C$  values to have an error between them smaller than  $10^{-8}$ . Once this is reached, it could be said that the  $N_{min}$  value is found; for instance, a plot of the error tendency can be seen below, so that error decreases as increasing  $N$ .

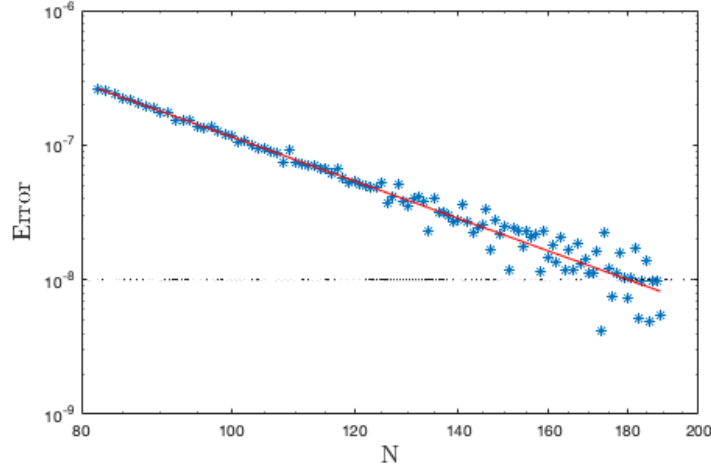


Figure 8: Convergence error for  $\lambda=0.5$  and  $\mu_\infty=0.0616$ , using equispaced nodes in finite elements with stencil 7.

Afterwards, the same methodology is carried out but for a slightly higher  $\lambda$  value; such that finally, convergence analysis has been performed for  $\lambda \in [0.5, 25]$  with small  $d\lambda=0.5$  increments. Moreover, the current study has also been completed for two different  $\mu_\infty$  values;  $\mu_\infty=0.0616$  corresponding to the blood shear viscosity at infinite shear rate and  $\mu_\infty=0.2$ , three times (approximately) the former one.

The ensuing figure displays the final minimum radial nodes  $N_{min}$  for each fluid time constant and for both  $\mu_\infty$  values. At first, it was expected to obtain an exponential dependency relation between  $N_{min}$  and  $\lambda$ , for higher  $\lambda$  higher  $N_{min}$ ; nevertheless, the surprising observed behaviour is by no means the former one. What can be witnessed is a staggered trend:

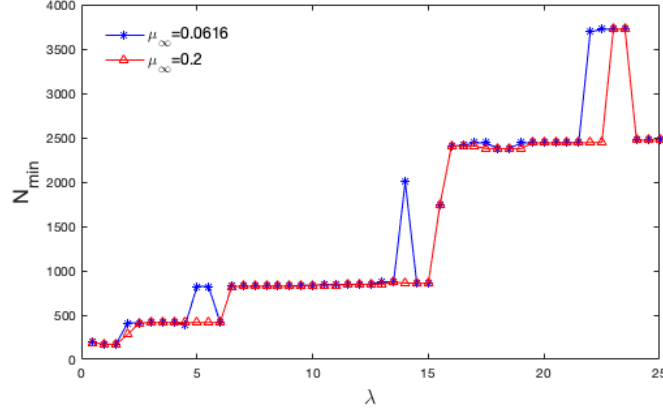


Figure 9: Minimum radial nodes ( $N_{min}$ ) required to fulfill viscosity convergence for different  $\lambda$  and  $\mu_\infty$  values.

This is due to the radial nodes position, which are not always placed in the most optimal spot to capture the exact viscosity behaviour; for instance, care must be taken concerning characteristics positions as inflection, maximum and minimum points, that is why in figure 8 the error points start to scatter at a certain point. Figure 10 shows that actually, using the minimum radial nodes found for each respective  $\lambda$ , the viscosity profile is well defined.

Summarizing, a high amount of radial nodes can be expected to be required to solve the problem for high fluid's time constants, which would be quite a problem for the blood scenario since the corresponding  $\lambda$ s are of the order of hundreds and thousands, as it will be seen. On the other hand, it should also be noted that Chebyshev discretization is not the most appropriate grid to use when solving the problem; however, a compromise has had to be found between the time required by the simulations and the discretization scheme accuracy in order to be able to consider the results as pleasant enough, without the need of spending many hours in the process.

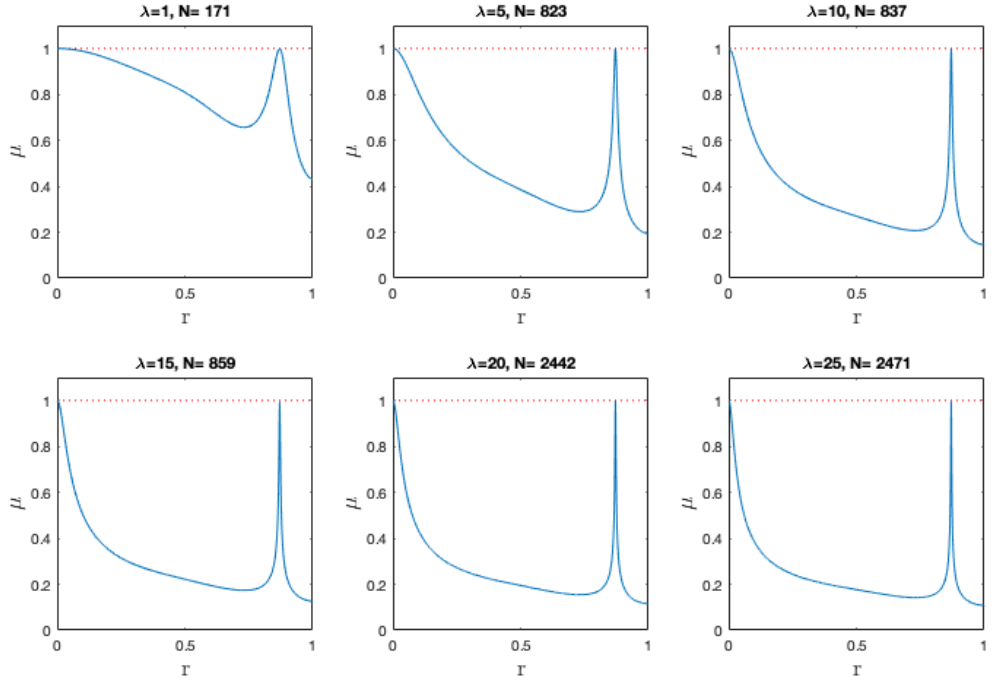


Figure 10: Viscosity profiles for different  $\lambda$  with each respective  $N_{min}$  required for a good shape definition.

## 6 Results and discussion

### 6.1 Base flow analysis

A blood base flow study has been carried out in this section in order to discover the blood laminar behaviour in different segments of the cardiovascular system, for both steady and unsteady base flows. For that reason, the descending aorta, left carotid artery and cerebral capillaries have been chosen to perform laminar flow profile simulation, with Carreau law modeling the blood viscosity. The following table shows the specific parameters for each cardiovascular section scenario after the corresponding research and adimensionalization process:

	$\hat{r}(m)$	$\hat{u}_{bmax}$ (m/s)	$\lambda$	$\mu_\infty$	$Wo$
D. Aorta	$1.6 \cdot 10^{-2}$	1.17	242.2631	0.0616	15
L. Carotid	$3.1 \cdot 10^{-3}$	$6.76 \cdot 10^{-1}$	722.4477	0.0616	5
Cerebral capillaries	$2.0 \cdot 10^{-6}$	$0.79 \cdot 10^{-3}$	1308.6350	0.0616	2

Table 4: Cardiovascular sections parameters

Before running the simulations, the held hypothesis was to expect a similar Newtonian blood behaviour in large arteries [7], as the shear-thinning effects due to the shear rate on the walls wouldn't be strong enough to affect the pipe center; while a flattened velocity profile was expected to be seen for the smallest vessels, for instance the cerebral capillaries, due to the more concentrated shear rate. However, the corresponding results are fairly surprising; a completely opposite behaviour is reflected.

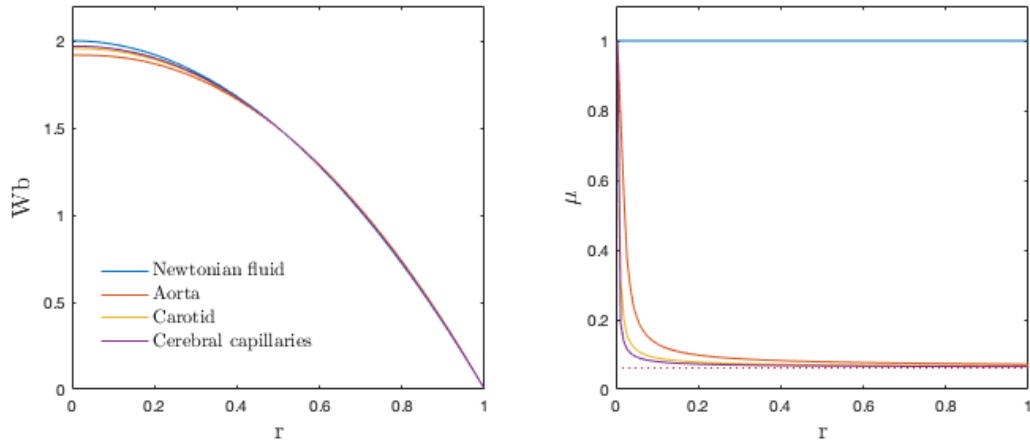


Figure 11: Blood steady laminar velocity and viscosity profiles.

The aorta blood (largest vessel) behaviour is the least similar to the Newtonian fluid; once the vessels start narrowing, the profile increasingly resembles the Newtonian case. The aforementioned is a consequence of  $\mu_\infty$  and  $\lambda$  values, as well as their respective relationship. In order to better understand what is happening, following steps refers to a parametric study.

It should be recalled that  $\mu_\infty$  is the fluid's viscosity at infinite shear rate, which means viscosity will converge to this  $\mu_\infty$  value for higher shear rate. Subsequently, the

convergence speed depends on parameter  $\lambda$ , which is the fluid's relaxation time; the higher the  $\lambda$  is, the faster the convergence to  $\mu_\infty$ . Therefore, for a fixed  $\mu_\infty$  (taken to be approximately three times the blood viscosity at infinite shear rate,  $\mu_\infty = 0.2$ ) and increasing  $\lambda$  (figure 12), the viscosity profile reaches faster the infinite shear-rate viscosity region, where the fluid behaves as a Newtonian one with viscosity  $\mu_\infty$ . Hence, as the transition region is also becoming narrower for higher  $\lambda$ s, the velocity profile does not have enough time to rearrange itself and resembles the Newtonian scenario, but with a lower viscosity. However, for lower  $\lambda$ s the fluid takes longer to reach the infinite shear rate region, which allows the velocity profile to readjust and to have a flattened shape, as it will be the  $\lambda = 5$  case.

The aforementioned could be also tested from another point of view: fixing  $\lambda$  and varying  $\mu_\infty$  (figure 13). In this case, decreasing  $\mu_\infty$  implies longer time for the fluid to reach the desired infinity shear-rate viscosity, so the fluid has more time to considerably change its velocity profile than for higher  $\mu_\infty$  values. Consequently, as  $\mu_\infty$  decreases, velocity profile stops resembling the Newtonian case and flattens out.

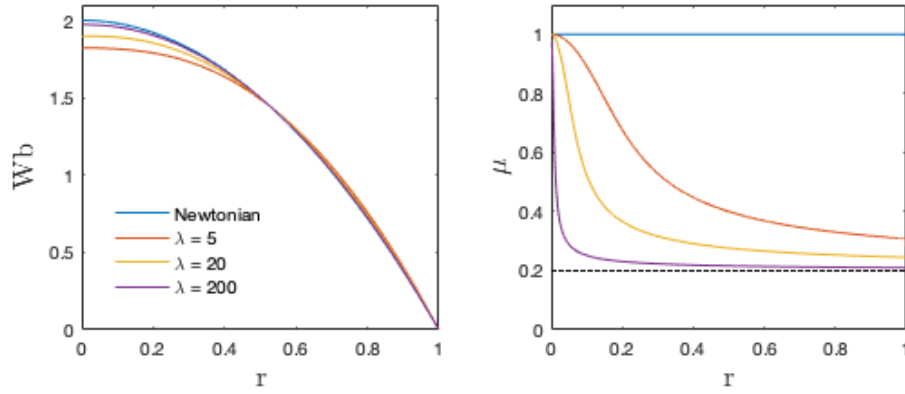


Figure 12: Base flow velocity and viscosity profiles for fixed  $\mu_\infty=0.2$ ,  $n_c=0.35$ ,  $a=2$ ,  $Re=2000$  and changing  $\lambda$

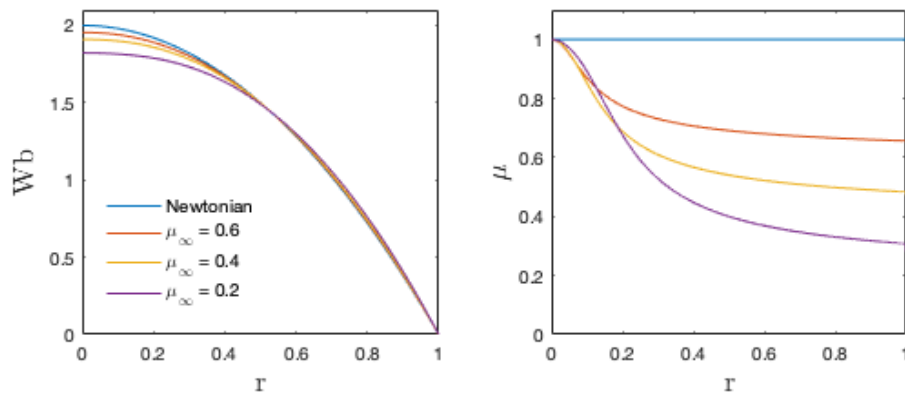


Figure 13: Base flow velocity and viscosity profiles for fixed  $\lambda=5$ ,  $n_c=0.35$ ,  $a=2$ ,  $Re=2000$  and changing  $\mu_\infty$

Ergo, it can be now understood why blood velocity profiles in different cardiovascu-

lar system sections look like in such a way. Table 4 display higher  $\lambda$  values for smaller vessels, with constant  $\mu_\infty$  (since in this study Carreau model is applied); then, it has been proved that when  $\lambda$  increases, viscosity reaches faster the infinite shear-rate viscosity region where the fluid resembles the Newtonian case with viscosity  $\mu_\infty$ , because the hasty transition region hasn't allowed it to rearrange itself into a much distinctive profile. So, that is why cerebral capillaries base flow resembles more the Newtonian case.

The same kind of study can be extrapolated to the pulsatile scenario. Therefore, different time instant profiles corresponding to specific conditions will be observed, such that the most remarkable flow features may be differentiated. For instance, one could start by analyzing what happens when the fluid time constant is fixed and  $\mu_\infty$  varies; in this case, the chosen  $\mu_\infty$  values correspond to  $\mu_\infty=0.0616$  (blood) and  $\mu_\infty=0.2$  (x3 blood).

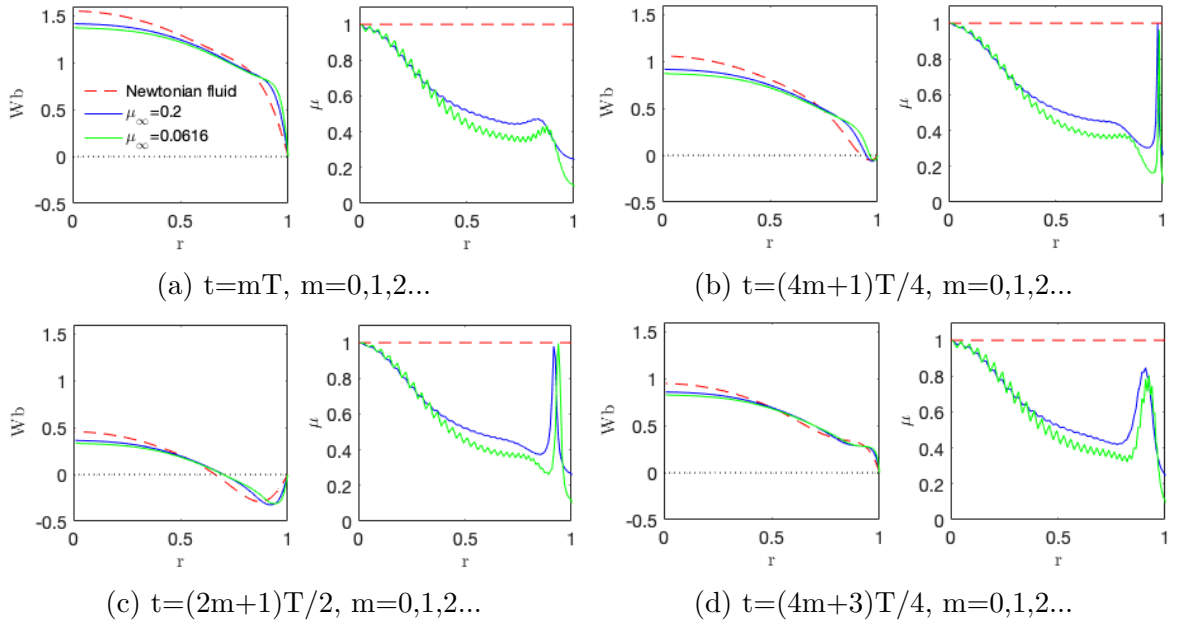


Figure 14: Velocity and viscosity profiles for  $\lambda=5$ ,  $Re=2000$ ,  $Wo=15$  and changing  $\mu_\infty$  for different times. Red dashed lines correspond to Newtonian case, blue and green to non-Newtonian case with  $\mu_\infty=0.2$  and  $\mu_\infty=0.0616$  respectively.

Regarding the velocity profile, a similar behaviour to the one observed for the steady case can be verified; for lower  $\mu_\infty$  values, more time is available for the fluid to reach the  $\mu_\infty$  viscosity and therefore, its profile differs more from the Newtonian case. However, a peculiar detail to highlight would be the behaviour near the pipe walls; a less smooth profile is witnessed compared to the Newtonian fluid and the appearance of several inflexion points are quite interesting for what they may entail in the future transient growth analysis. Moreover, for lower  $\mu_\infty$  values, narrower and more exaggerated the new behaviour near the walls is.

On the other hand, the corresponding viscosity profiles for each chosen time instant are plotted. As it can be readily seen, the accuracy is not as pleasant as expected; this is due to the radial nodes (Chebyshev,  $N=80$ ) used in the spatial discretization, whose impact has been deeply studied and explained in the previous section of Convergence

Analysis. Besides, as the time goes on, the viscosity profile evolution is captured in the previous plots, exposing peculiar peaks near the walls that were not previously seen in the steady scenario.

Facing the problem from another point of view could be fixing  $\mu_\infty$  and changing the fluid's time constant  $\lambda$ . The witnessed behaviour in the pulsatile scenario shows more clearly the shear-thinning effects than in the steady state; the velocity profile acquires a flatter profile and moreover, with a special shape near the walls. In particular, the higher the  $\lambda$  values are, the steeper the profile becomes near the boundaries. What is more, this behaviour with respect to  $\lambda$  is maintained for different  $\mu_\infty$ , Womersley and Reynolds.

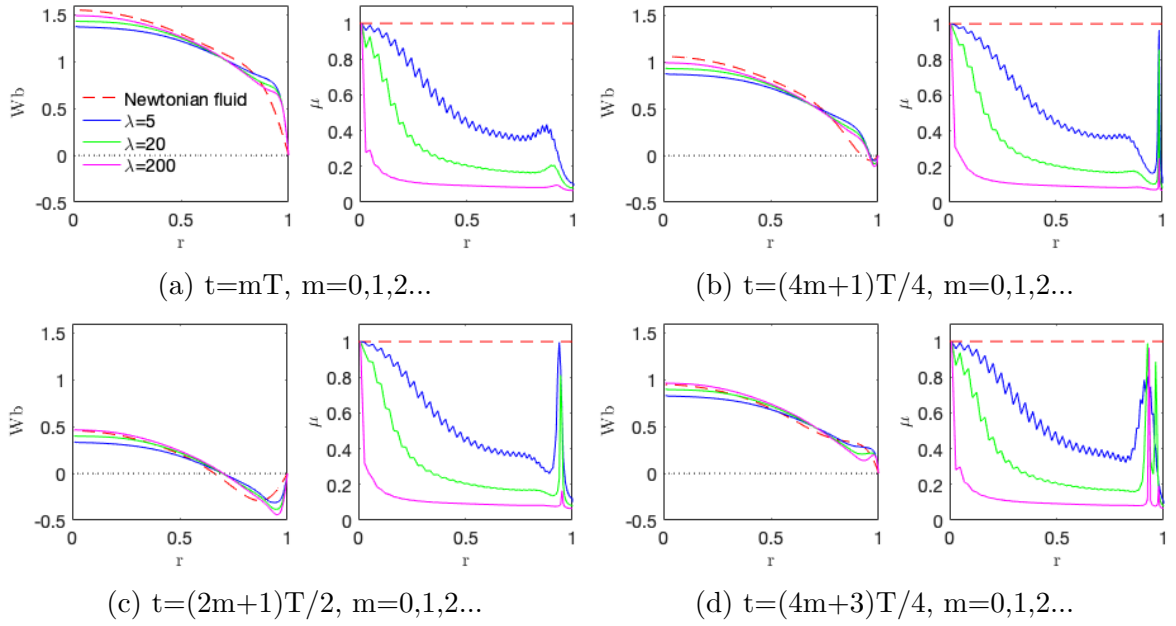


Figure 15: Velocity and viscosity profiles for  $\mu_\infty=0.0616$ ,  $Re=2000$ ,  $Wo=15$  and changing  $\lambda$  for different times. Red dashed lines correspond to Newtonian case; blue, green and pink to non-Newtonian case with  $\lambda=5$ ,  $\lambda=20$  and  $\lambda=200$  respectively.

In addition, it should be taken into account that for the unsteady pulsatile base flow the new parameter  $Wo$  (Womersley number) appears, such that it could be deduced both velocity and viscosity profiles depend on it too. Indeed, the dependency would be as depicted in figure 16; decreasing  $Wo$  leads to a softer velocity profile whose viscosity peculiar peaks shift slightly farther from the pipe wall, as the inflection points, maximums and minimums in the velocity profile move towards the pipe center. This behaviour makes sense since higher  $Wo$  means less viscous effects (remember Womersley relation:  $Wo = D/2\sqrt{w/\nu}$ ) so the flow does not have as much resistance and can acquire a steeper profile than the ones for low Womersley.

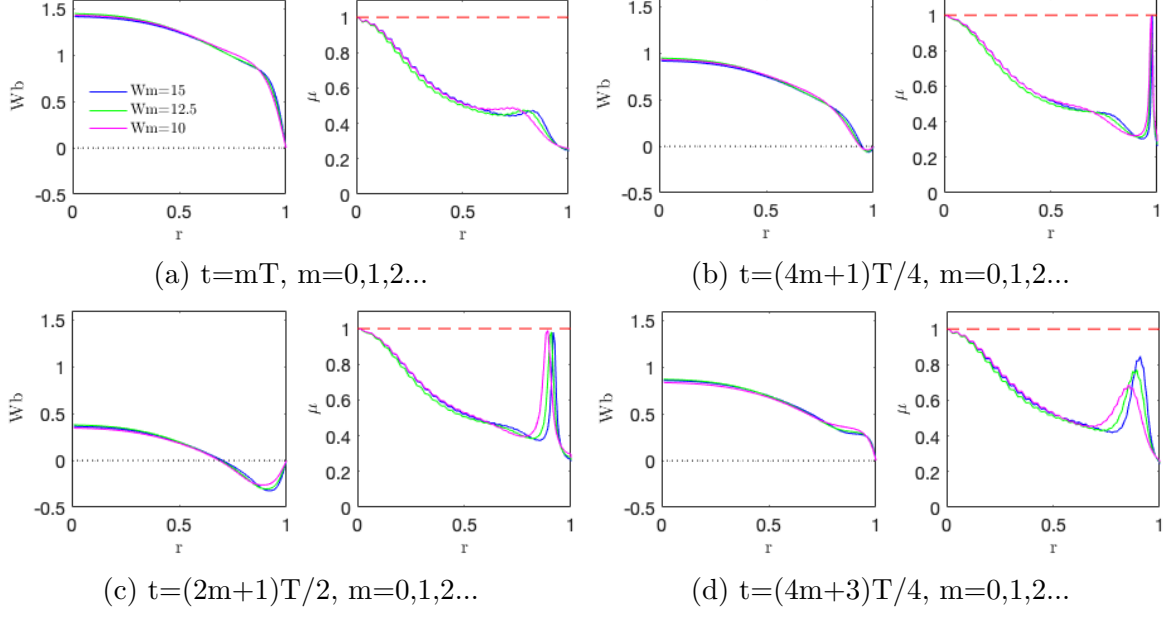


Figure 16: Velocity and viscosity profiles for  $\lambda=5$ ,  $Re=2000$ ,  $\mu_\infty=0.2$  and changing  $Wo$  for different times. Red dashed lines correspond to Newtonian case; blue, green and pink to non-Newtonian case with  $Wo=15$ ,  $Wo=12.5$  and  $Wo=10$  respectively.

Finally, unsteady base flow profiles for the same cardiovascular sections presented at the beginning of this section (descending aorta, left carotid and cerebral capillaries) have also been computed. Different fluid time constants and Womersley numbers describe the blood problem, the only fixed parameter in this case is the infinite shear-rate viscosity.

Even if we could expect a softer profile for the descending aorta, because it has the lowest time constant, what is actually seen is the narrowest behaviour near the wall. This is due to Womersley number, which is higher, and its influence on the profile shape is stronger than  $\lambda$ 's one. On the other side, cerebral capillaries are the ones with highest  $\lambda$  but lowest  $Wo$ , so the profile is the softest among all.

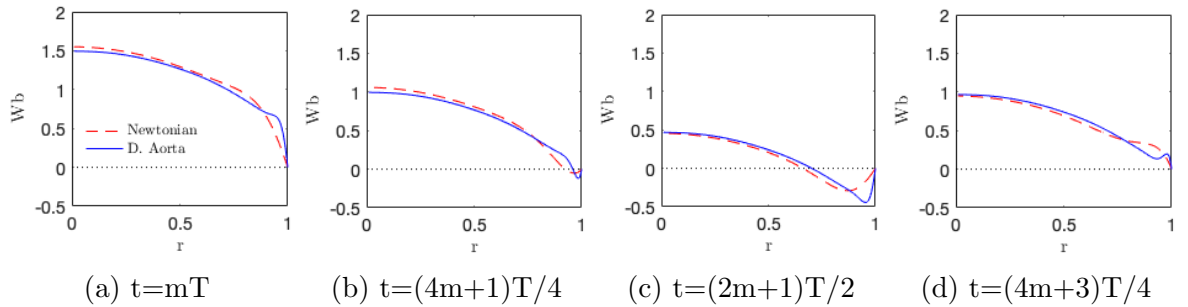


Figure 17:  $m=0,1,2,\dots$  Pulsatile base flow Descending Aorta velocity profiles for different instants.  $\lambda=242.2631$ ,  $\mu_\infty=0.0616$  and  $Wo=15$ . Red dashed and blue lines correspond to Newtonian fluid and Desc. Aorta respectively.



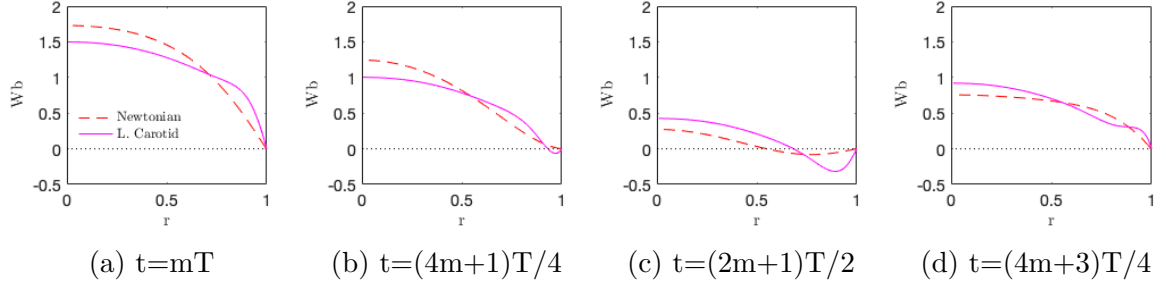


Figure 18:  $m=0,1,2,\dots$  Pulsatile base flow Left Carotid Artery velocity profiles for different instants.  $\lambda=722.4477$ ,  $\mu_\infty=0.0616$  and  $Wo=5$ . Red dashed and pink lines correspond to Newtonian fluid and Left Carotid Artery respectively.

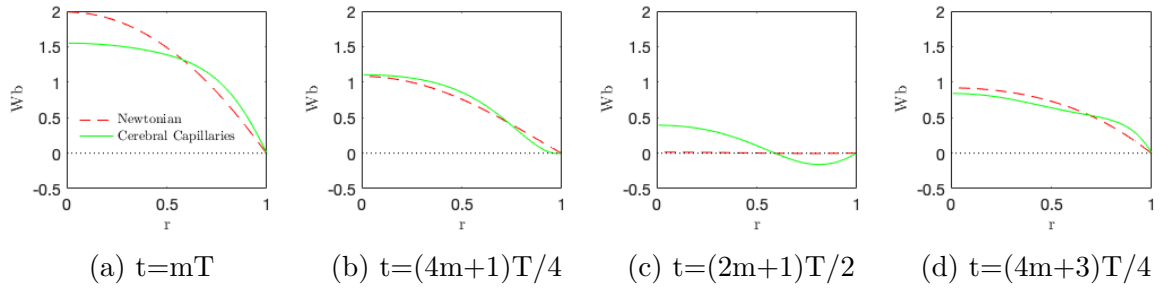


Figure 19:  $m=0,1,2,\dots$  Pulsatile base flow Cerebral Capillaries velocity profiles for different instants.  $\lambda=1308.6350$ ,  $\mu_\infty=0.0616$  and  $Wo=2$ . Red dashed and green lines correspond to Newtonian fluid and Cerebral Capillaries respectively.

## 6.2 TGA results

So far, how to approach the problem and a deep review of what is happening with pipe base flow for a non-Newtonian fluid, as the blood, have been seen. Following, in this section, the TGA results are analysed and discussed. However, before directly addressing the results, a brief refresh could be useful. The Transient Growth Analysis method performs a non-modal stability analysis making use of the linearized Navier Stokes equations and assuming small enough flow perturbations; linearization has been performed for Newtonian and non-Newtonian disturbances (as seen in section 4.3). Thus, in this framework the perturbations grow through linear mechanisms on top of the base flow profile.

So, the most dangerous initial velocity perturbation is computed using TGA in terms of energy growth, out of a wide range of azimuthal and axial wavenumbers, is to say, out of all initial perturbation shapes, initial ' $t_0$ ' and final ' $t_f$ ' pulsation phases; such that the larger this energy gain is, the easier the transition to turbulence will be.

Newtonian and non-Newtonian perturbations on top of the same base flow, for small fluid's time constants, have been analyzed; what is captured is basically the same optimal disturbance. The helical shape is preserved for both scenarios, as well as the initial and final phase to obtain maximal growth. The only term that differs concerns the energy growth, such that non-Newtonian perturbation is slightly more amplified than the Newtonian one (see table 5). However, as the results are quite the same, proved with the following figures (20 and 21), and it is known that for higher

$\lambda$  the viscosity problem is not completely well defined and it would require too many discretization nodes, hereafter only Newtonian perturbations on top of non-Newtonian base flows are considered.

For the following table concerning the Newtonian and non-Newtonian perturbations TGA results, remember that  $\alpha$  and  $\beta$  stand for axial and azimuthal wavenumbers respectively.

	$G_{max}$	$\alpha$	$\beta$	$t_0/T$	$t_f/T$
Newtonian	1064.6160	3	1	0.3	1
non- Newtonian	1104.7449	3	1	0.3	1

Table 5: Newtonian and non-Newtonian perturbations TGA results.

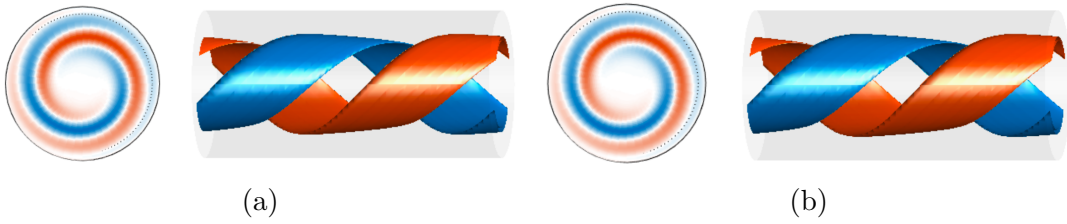


Figure 20: Optimal (a) Newtonian and (b) non-Newtonian perturbations at maximal growth ( $t=1T$ ) on top of non-Newtonian base flow with  $\lambda=0.06$ ,  $Wo=15$ ,  $Re=2000$ ,  $A=1$ ,  $a=2$ ,  $n_c=0.35$  and  $\mu_\infty=0.2$ .

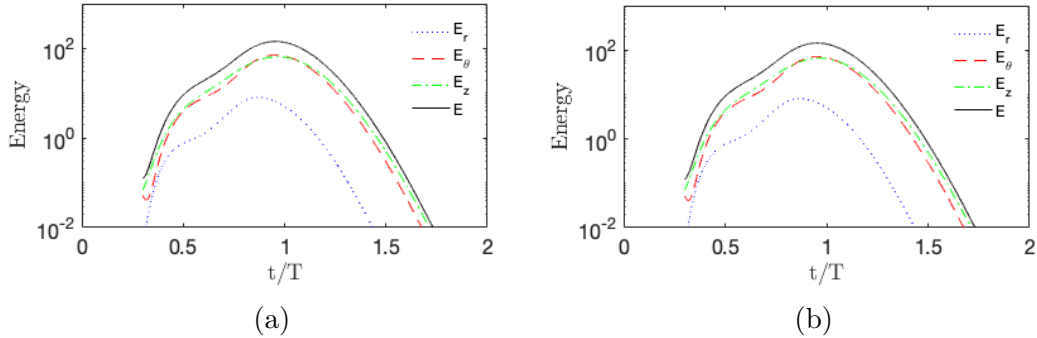


Figure 21: Energy plot for (a) Newtonian and (b) non-Newtonian perturbations on top of non-Newtonian base flow with  $\lambda=0.06$ ,  $Wo=15$ ,  $Re=2000$ ,  $A=1$ ,  $a=2$ ,  $n_c=0.35$  and  $\mu_\infty=0.2$ .

Hence, the dependence of the Newtonian perturbation energy gain with respect of the different parameters that define the flow could be analyzed to highlight the most important features. Starting with Reynolds number, one could verify that for higher  $Re$  the maximum gain  $G_{max}$  is also remarkably higher, fact that has already been proven at previous works as Duo Xu et al. [6] for Newtonian base flows. Thinking about this result plus remembering that Reynolds number is defined by  $Re=uD/\nu$ , a logical explanation can be found: higher  $Re$  implies lower  $\nu$ , is to say, less viscous effects, such

that the perturbation has more freedom and less resistance to develop and amplify itself (see figure 23 (a)).

Concerning the Womersley number, the behaviour is now the opposite: for higher  $Wo$  ( $Wo > 10$ ), less amplification. This can be related with the optimal perturbation shape; it has been proven that lower  $Wo$  corresponds to helical perturbation shapes (for all  $\lambda$  values), while higher  $Wo$  lead to stream-wise geometries, the classical one, also for all  $\lambda$  values. Therefore, it could be deduced that in a certain point, as Womersley number and  $\lambda$  increase, a change in the perturbation shape (from helical to stream-wise) will be perceived. After a proper parametric analysis it has been found when this shape alteration occurs, for two different scenarios: for  $\mu_\infty=0.0616$  the perturbation reshaping takes place at  $Wo=10$  and  $\lambda \in [5,20]$ ; and for  $\mu_\infty=0.2$  the perturbation modulation takes place at  $Wo=12.5$ , also in the fluid's time constant range  $\lambda \in [5,20]$ . So, as well as in [6], for sufficiently large  $Wo$  the classic disturbance dominates and the optimal gain  $G$  of steady pipe flow is recovered.

A graphic representation is attached in the following figures, for  $\mu_\infty=0.0616$ ,  $Wo=10$  and  $Re=2000$  scenario.

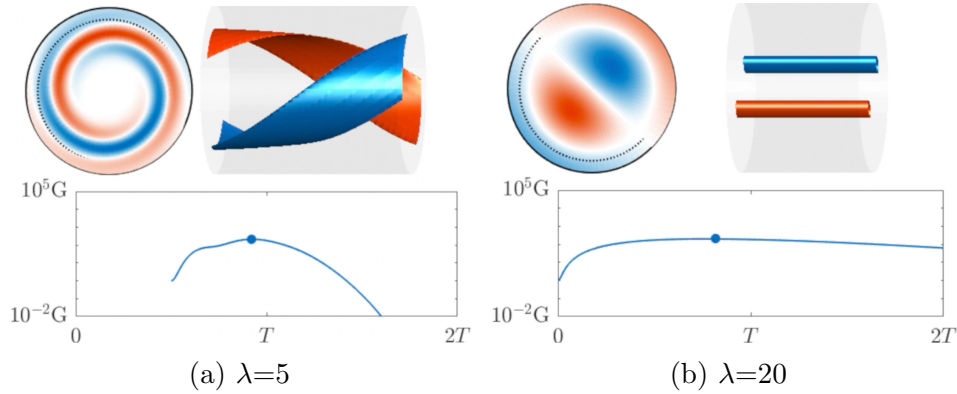


Figure 22: Upper right plot: Optimal perturbations at maximal energy growth for (a)  $\lambda=5$ ,  $t=0.9T$  and (b)  $\lambda=20$ ,  $t=0.8T$ . Upper left plot: contour of vorticity on a  $r-\theta$  cross-section. Bottom plot: time series of the energy growth of the optimal (a) helical  $(\alpha,\beta)=(3,1)$  and (b) classic  $(\alpha,\beta)=(0,1)$  disturbances at  $(Re,A, Wo)=(2000,1,15)$ .

For the parameter values of figure 22 (a), the optimal disturbance has a helical structure with  $(\alpha,\beta)=(3,1)$  and is localized at the outer half of the pipe. The optimal point to disturb is during the deceleration phase at  $t_0=0.5T$ , as well as the maximum amplification is reached also during the deceleration phase at  $t_0=0.9T$ . In this case, the kinetic energy of the optimal helical perturbation is mostly distributed in the stream-wise and azimuthal components (which indicates a strong three-dimensional effect), which self-amplify rapidly during the deceleration phase and start decaying from  $t=0.9T$  on. Initially the disturbance spirals clock-wisely towards the pipe center; as the energy grows, the perturbation switches the spiraling direction.

The classic  $\alpha=0$ ,  $\beta=1$  optimal disturbance observed in figure 22 (b) consists of stream-wise vortices, which means the energy is subsequently transferred to the stream-wise velocity components, while the cross-stream ones decay monotonically. Overall the classic perturbation's behavior appears to be rather insensitive to the change in flow profile throughout the cycle and the decay is very slow. In fact, this tendency was already noticed by Duo Xu et al. [6].

The aforementioned result regarding the change of geometry for different  $\mu_\infty$  may lead to deduce that the energy gain depends on the infinite shear rate viscosity too. Figure 23 (c) clearly shows the corresponding relationship between  $G$  and  $\mu_\infty$ ; for lower viscosity values, less energy gain, so less danger to trigger transition to turbulence. Moreover, this result agrees with the one above, such that lower viscosity values correspond to lower energy amplifications; this could entail a sooner perturbation geometry change.

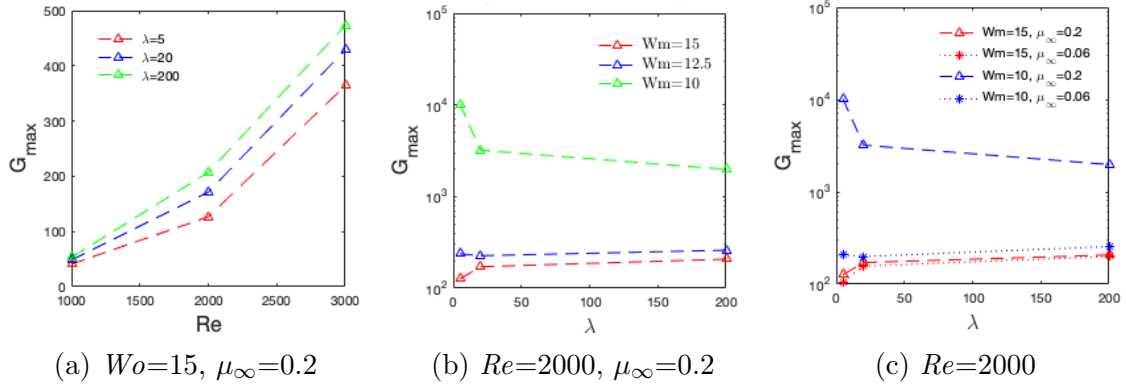


Figure 23: Maximal energy growth with respect (a) Reynolds number for different  $\lambda$ , (b) fluid's time constant for different  $Wo$  and (c) fluid's time constant for different  $Wo$  and  $\mu_\infty$ .

Finally, moving to the blood scenario one should pay more attention on the Descending Aorta cardiovascular section, since it is the one where turbulence transition is most critical regarding deaths.

It has been found that the most dangerous perturbation, which can trigger easily transition to turbulence, consists of stream-wise vortices. This outcome completely agrees with the result previously found; perturbation geometry change from helical to classic disturbance for  $\mu_\infty=0.0616$  (blood scenario) occurs at  $Wo=10$ , and actually the descending aorta works for higher Womersley, as seen in the following table.

	$\lambda$	$\mu_\infty$	$Wo$	$G_{max}$	$\alpha$	$\beta$	$t_0/T$	$t_f/T$
Desc. Aorta	242.2631	0.0616	15	201.2604	0	1	0	1.7

Table 6: Desc. Aorta parameters and TGA results for the most dangerous perturbation to trigger turbulence transition.

Figure 24 (b) shows that the energy is transferred to the stream-wise velocity component, while the cross-stream components decay quickly and monotonically. The optimal point to disturb is during the acceleration phase, specifically just at the beginning of the period, and the maximum energy amplification is reached at the deceleration phase, after 1.7 periods from the initial phase:  $t_f=1.7T$ . Finally, figure 25 displays the 3D perturbation shape at its maximum energy amplification point and contour vorticity on a  $r-\theta$  cross-section.

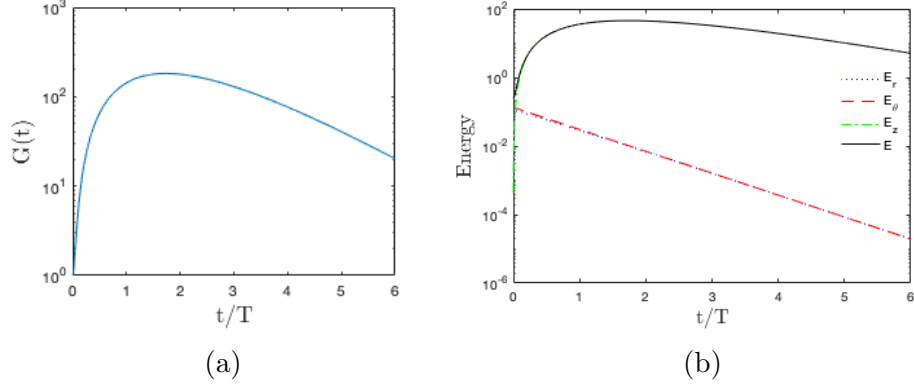


Figure 24: (a) Energy growth of the optimal stream-wise disturbance at  $(Re, A, Wo) = (2000, 1, 15)$  for the desc. aorta  $\lambda = 242.2631$  and  $\mu_\infty = 0.0616$ . (b) Time series of kinetic energy contribution of each velocity component for the optimal disturbance.

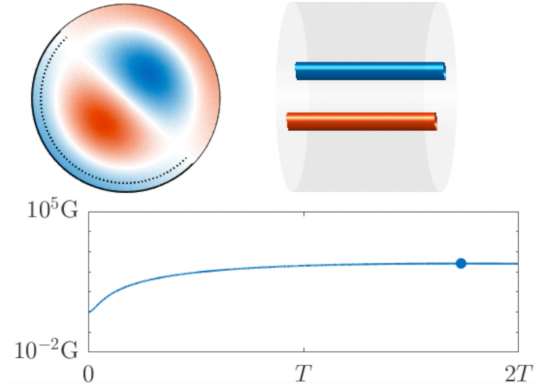


Figure 25: Optimal perturbation at maximal energy growth ( $t_f = 1.7T$ ) for the descending aorta  $\lambda = 242.2631$ ,  $\mu_\infty = 0.0616$ . Upper left plot: vorticity contour on a  $r-\theta$  cross-section. Bottom plot: time series of the energy growth for two periods.

## 7 Conclusions

To put the whole project in a nutshell, I could gladly state that the main goals have been successfully fulfilled. For instance, the state of the art study led us to use the Carreau-Yasuda model to approximate the viscosity behaviour; this model has been proven to be exceptionally outstanding for the steady driven case. Surprisingly, after the pulsatile flow study, Carreau-Yasuda law has turned out to not really be a good model to approximate the blood flow problem. This is because the corresponding shear-thinning blood parameters ( $\hat{\mu}_0, \hat{\mu}_\infty, n_c, a, \hat{\lambda}$ ) are determined from steady driven experiments (not for time dependent flows) where shear-thinning is applied until the flow stabilizes; after that, the results are fitted in a curve which meets the model. So, to get a better approximation for the blood flow problem, one should take into account new parameter values which fit the pulsatile scenario and other blood properties, as it could be the viscoelasticity.

Referring to the practical part of the project, base flow Matlab codes have been implemented with flying colours, validating them with previous works as the one from Xu et al. [6] for Newtonian fluids and with Lopez-Carranza paper [15] for steady non-Newtonian case. What is more, the unsteady non-Newtonian case has also been covered and it has been discovered that the dimensionless fluid's time constant  $\lambda$  parameter has a huge impact on the laminar flow profile, which later will also be crucial for Transient Growth Analysis. Concerning the unsteady pulsatile case, the new parameter, Womersley number, takes possession and it is basically the one which rules the velocity profile and consequently, the viscosity profile, which has let us notice that Chebyshev discretization grid is not the best one to treat the problem, but using finite elements.

Finally, Transient Growth study has uncovered that Newtonian and non-Newtonian perturbations introduce quite the same danger concerning turbulence transition (for small lambdas) in non-Newtonian base flows, such that the energy gain behaviour with respect Reynolds and Womersley numbers is the same as found by Duo Xu et al. [6]. For higher Reynolds, higher energy amplification and for higher Womersley, lower gain.

Last but not least, despite the model's limitations, the most important goal of this project was to find the most dangerous perturbation for turbulence transition in the descending aorta, in view of the fact that it is the cardiovascular section where turbulence is most critical regarding deaths. The optimal perturbation has turned out to be a stream-wise disturbance with maximum amplification after 1.7 periods since its introduction in the base flow.

I truly think this research line is of deep importance in order to better understand what is going on in our vessels and also to be aware and try to prevent misfortunes. However further work and model improvement are still left to be done as a means to properly describe the problem and to be able to suitably modelize real blood behaviour; starting from choosing an upgraded non-Newtonian viscosity model, until an appropriate discretization scheme that can actually capture the precise blood behaviour.

## References

- [1] Gotlieb AI. Cunningham KS. *The role of shear stress in the pathogenesis of atherosclerosis*. Lab Invest., 2005.
- [2] Michael Eckert. *Pipe flow: a gateway to turbulence*. Springer, 2020.
- [3] A. M. Robertson et al. *Rheological models for blood*. Springer, 2009.
- [4] A. Meseguer et al. *Linearized pipe flow to Reynolds number  $10^7$* . Journal of Computational Physics, 2003.
- [5] D. Barkley et al. *Direct optimal growth analysis for timesteppers*. International Journal for numerical methods in fluids, 2008.
- [6] Duo Xu et al. *Non-modal transient growth of disturbances in pulsatile and oscillatory pipe flow*. Journal of Fluid Mechanics, 2020.
- [7] J. S. Horner et al. *Investigation of blood rheology under steady and unidirectional large amplitude oscillatory shear*. The Society of Rheology, 2018.
- [8] M. Armstrong et al. *Evaluating rheological models for human blood using steady state, transient, and oscillatory shear predictions*. Springer, 2018.
- [9] N. Bessonov et al. *Methods of Blood Flow Modelling*. EDP Sciences, 2016.
- [10] P.J. Schmid et al. *Stability and Transition in Shear Flows*. Springer Science and Business Media New York, 2001.
- [11] R. Trip et al. *An experimental study of transitional pulsatile pipe flow*. American Institute of Physics, 2012.
- [12] S. Hugues et al. *An improved projection scheme applied to pseudospectral methods for the incompressible Navier-Stokes equations*. Int. J. Numer. Meth. Fluids, 1998.
- [13] S. Tabakova et al. *Application of the Carreau Viscosity Model to the Oscillatory Flow in Blood Vessels*. AIP Conf. Proc., 2015.
- [14] S. Tabakova et al. *Oscillatory Carreau flows in straight channels*. Royal Society Open Science, 2020.
- [15] S.N. López-Carranza et al. *Pipe flow of shear-thinning fluids*. C.R. Mecanique, 2012.
- [16] Derek Jackson and Brian Launder. *Osborne Reynolds and the Publication of His Papers on Turbulent Flow*. Annu. Rev. Fluid Mech., 2007.
- [17] M. A. Leschziner and D. Drikakis. *Turbulence modelling and turbulent-flow computation in aeronautics*. The Aeronautical Journal, 2002.
- [18] John Lumley and Peter Blossey. *Control of Turbulence*. Annu. Rev. Fluid Mech., 1998.
- [19] I. Newton. *Newton's Principia : the Mathematical Principles of Natural Philosophy*. New-York :Daniel Adee, 1642-1727.

- [20] World Health Organization. The top 10 causes of death.
- [21] A. Sequeira and J. Janela. *An overview of some mathematical models of blood rheology*. Springer, 2007.
- [22] Lloyd N. Trefethen. *Spectral methods in Matlab*. SIAM, 2000.